Amplifying Exploration of Regional Climate Risks: Clustering Future Projections on Regionally Relevant Impact Drivers Not Emission Scenarios

Franciscus Eduard Buskop[1,2], Frederiek Sperna Weiland[2] and Bart van den Hurk[1,2]

[1] Institute for Environmental Studies, Vrije Universiteit Amsterdam, Amsterdam, The Netherlands
[2] Deltares, Delft, The Netherlands

E-mail: t.buskop@vu.nl

Abstract

Climate impacts will continue to evolve over the coming decades, requiring regions worldwide to obtain actionable climate information. Global Climate Models (GCMs) are often used to explore future conditions, but the variability of projections among GCMs complicates regional climate risk assessments. This variability in future projections is only partly explained by the often-used emission scenarios. Model uncertainty and internal variability play a major role in the outcomes of projected meteorological conditions, especially for local precipitation patterns. As precipitation is a key driver for hazards such as floods, droughts, and wildfires, local assessment of resulting risks using emission-based multi-model means probably leads to limited impact exploration. This study proposes a method to select more impact-relevant scenarios by determining regionally relevant climatic impact drivers and clustering GCMs on their projected changes in these drivers. We quantify the effectiveness of our approach by comparing future impacts covered by multi-model means per emission scenario with our approach, expressed as an "exploratory amplification" factor. We illustrate the method for flood risk in the Latvian Lielupe basin and find the novel method has an exploratory amplification up to a factor of eight for the mid-century. We conclude that our method results in locally relevant climate scenarios that significantly improve regional exploration of future climate impacts. Such scenarios provide targeted risk information that can be used in adaptation planning.

1. Introduction

In the decades of the mid-twenty-first century, the impacts of a changing climate will increasingly emerge. (Mora et al., 2013). Therefore, regions worldwide must start taking inventory of their future climate risks and have societal discussions on their adaptation efforts. Although many global risk assessments exist, translating global assessments of climate risks to a regional level remains challenging. Global impact studies can help set the agenda, but regional action requires more locally specific information (Blankespoor et al., 2023). Meanwhile, at a regional level, available resources may be limited (Measham et al., 2011) to process the large volume of climate data from large model intercomparison projects.

Even though resources are limited, there is a need to analyse multiple GCM outcomes to capture the vast variability of regional climate change features. In particular, changes in rainfall patterns – driving natural hazards like flooding (Merz et al., 2021), drought (Cook et al., 2020) and wildfires (El Garroussi et al., 2024) or crop failures (Goulart et al., 2021) – display large uncertainties that are a complicating factor in risk planning. For instance, flood impacts can vary significantly over different climate model ensembles (Rojas et al., 2013).

The combination of limited local resources combined with uncertainty in climatic impact drivers (CIDs) (Ruane et al., 2022) emphasises the need to obtain a broad picture of potential future impacts while limiting the number of scenarios needed to analyse. An often-used approach to handle projection uncertainty is to use multi-model means of emission-based scenarios used in the IPCC reports, such as a representative concentration pathway (RCP), socio-economic pathway (SSP), or Global Warming Level (GWL). Taking means allows for a robust signal of climatological trends and reduces the number of scenarios needed to analyse for policy making. In recent years, many policymakers have become accustomed to these types of scenarios. However, emission scenarios only explain about 15% of total precipitation variance in CMIP6 by the end of the century on a global level (Lehner et al., 2020) and 5-10% of European winter precipitation in CMIP5 (Hawkins & Sutton, 2011). For the mid-century, the emission scenarios can explain even lower fractions of the total variance. Reasons for lower fractions in the mid-century compared to the end of the century are due to the large inertia of the climate system and multiple modes of internal variability that complicate the detection of forced climate response for the near to medium-term (Samset et al., 2020; Tebaldi & Friedlingstein, 2013). As a result, projected precipitation change in the various multi-model means of emission scenarios are very similar. It is hypothesised that the impacts of these mean changes are then also similar across the emission scenarios. As a result, regions could spend their limited resources on the analysis of scenarios that highlight only a very limited risk range. Their collection of scenarios has limited exploratory power. Enhancing insight into the future climate risk range can help regions better prepare for an uncertain climate future. This gives rise to the question: Are there better ways to highlight the spread of potential climate risks at the local level?

This paper presents a three-step framework to increase the exploratory power of future climate scenarios. We do this by creating 'impact-oriented climate information' (van den Hurk, 2022) by spanning the range of future conditions, taking into account regional uncertainty in climate change responses of locally relevant CIDs. The three-step process first identifies the climate challenge, the region and the timeframe of interest. Then, the most relevant CIDs in the region are determined. Afterwards, new impact-oriented climate scenarios are defined based on the GCM projections of the relevant climate features. Lastly, we examine the framework's effectiveness in representing a diverse range of possible outcomes for an impact category while keeping the number of scenarios low. This is done by comparing the exploratory power of the set of emission-based scenarios versus impact-relevant scenarios.

The framework is illustrated using a riverine flood example. Flooding is one of the four key risks in Europe, and regions will need to implement measures to prevent increases in damages and the number of people affected (Bednar-Friedl et al., 2022). The example covers the Lielupe basin, which spans 17.600 km² across Lithuania and Latvia. The area covers 13.8% of Latvian territory and is home to about 400.000 inhabitants. Latvian authorities have identified the land area around the Lielupe river as a flood-risk area of national importance. Therefore, the study explores how climate change impacts flood discharges in the current flood area. The changes in 100, 50 and 20-year return period discharges are defined as guiding impact metrics to explore future flood risk.

2. Methods

This section introduces the data and methods that make up the scenario selection procedure (Figure 1) to explore the future risk range with limited scenarios. First, we describe the region and the hydrological model. Second, we elaborate on the selection of the climate region and the timeframe of interest (step 1). Third, we describe the method to obtain relevant CIDs (step 2). Then, we detail how GCM projections are clustered into impact-oriented climate scenarios (step 3). Lastly, the exploratory power of impact-oriented scenarios is compared to that of emission-based model mean scenarios.
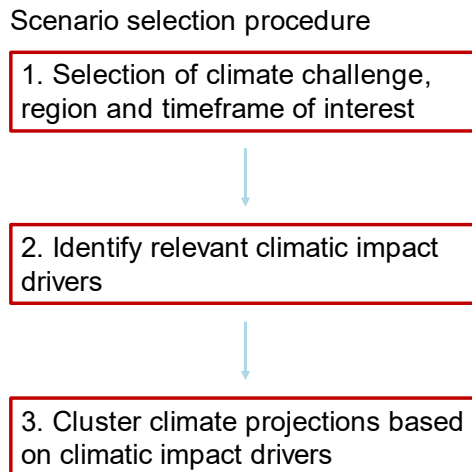
Scenario selection procedure

Figure 1: General framework used in the study to obtain impact-relevant climate scenarios. The application to the case study is detailed in the text.

2.1 Study area and hydrological modelling

The area of interest, shown in Figure 2, is a basin in the Baltic States region of Europe. Although precipitation amounts in the region are higher during summer than in winter, the catchment is characterised by seasonal high flows in the spring period. However, with potential increases in mean precipitation and its variability (expressed as larger changes in the extremes compared to changes in the mean) in the summer period (see Figure B.10), this study also considers the possibility of future high flows in the summer.

The hydrological model used is the distributed hydrological model wflow_sbm (van Verseveld et al., 2024). This is set up using wflow_sbm model builder HydroMT, which combines openly available global datasets to develop first-order models for any basin in the world (Eilander et al., 2023). The used model serves as a tool to make a quick scan of the climate variables that influence high-discharge statistics the most. This study does not consider ice jams in rivers, which can be a cause of flooding in the region. The model runs on a daily timestep with a resolution of 0.00833x0.00833° per grid cell (locally ~925x515m). To validate the model, historically observed discharges are compared with those reconstructed by forcing the hydrological model with historical ERA5 reanalysis of 0.25x0.25° (locally ~27.8x15.2km) resolution (Hersbach et al., 2023) between June 1950 and June 2023. The observational data is retrieved from local authorities (Latvian Environment, Geology and Meteorology Centre) and the World Meteorological Organization Global Runoff Data Centre (GRDC). Overall, the modelled discharges have a fair correspondence with the historical record for various stations in the basin. For more details, see Appendix A.

For the impact variables, discharges at Mezotne station are taken due to its proximity to high flood-risk areas identified by local authorities. We aim to capture changes in high flows with a return period of 20, 50 and 100 years (also referred to as RP20, RP50 and RP100).
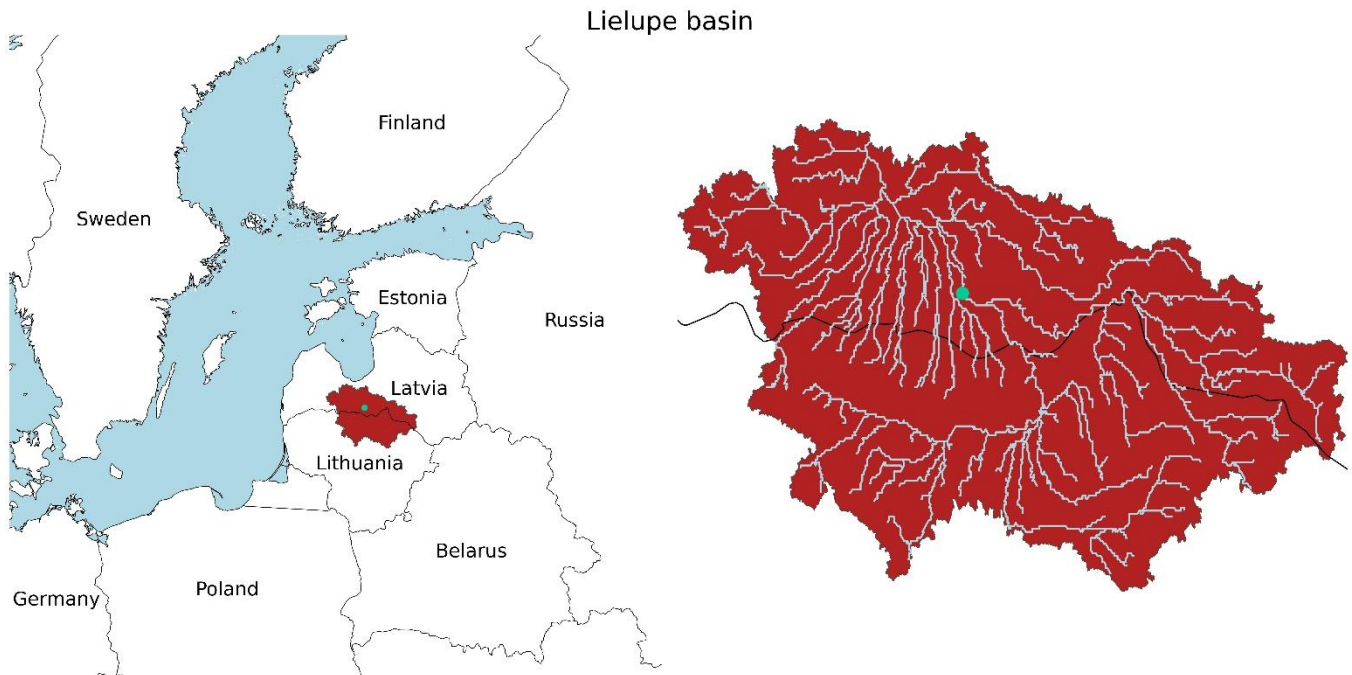
Figure 2: Region of interest. The red-filled shape is the Lielupe basin, the green dot indicates the discharge station Mezotne, and light blue indicates the sea surface and the rivers. The left panel shows the location in Europe and the right panel is a more detailed image of the river network in the basin.

2.2 Selection of climate region and timeframe of interest

Since the Lielupe basin is small and, therefore, subject to large internal variability in the observed and modelled weather, getting a climate signal can be challenging. To retrieve a more robust signal of the climatological changes in the area, a larger region of interest has been defined to extract climate features from (See Figure 3). This region is selected by analysing monthly average precipitation and temperature in Europe with the ERA5 dataset between 1940-2024. We filtered the area on grid cells that have a correlation higher or equal to 0.60 to the grid cell at the centre of the basin. If the correlation area for temperature and precipitation differs, the smallest area is selected.

In this study, we select three timeframes of interest to explore how the scenarios develop over time and compare them to the development of the emission-based model over time. However, in other studies, a timeframe can be selected depending on the decision-maker's planning horizon. The three selected timeframes are: near-term 2021-2040, mid-century 2041-2060, and end-of-century 2081-2100. These timeframes coincide with those used in the IPCC Atlas (Gutiérrez et al., 2021).

2.3 Identify impact-relevant climate features

For the second step in defining impact-relevant climate scenarios, we determine the relevant CIDs for the region. We follow the exploratory modelling and analysis principle (Bankes, 1993; Bankes et al., 2013), where uncertainties are systematically sampled to find those of highest influence on the outcomes of interest. The decision-scaling method (Brown et al., 2012) is an exploratory modelling and analysis method which we will follow in this paper to find relevant CIDS. The method has been successfully used in water resource (Steinschneider, McCrary, et al., 2015) and flood studies (Spence & Brown, 2016). The method allows us to sample hydro-meteorological uncertainties of GCM projections and relate them to hydrological impacts. This method uses a stochastic weather generator based on Steinschneider and Brown (2013) to generate weather time series for current-day (baseline) and future climate conditions. Future time series are made by adjusting selected climate features in the baseline series. Using the baseline and future climate weather time series, we generate discharges using the hydrological model introduced in section 2.1 and compare discharge extremes in the future climate realisation against the extremes resulting from the baseline weather time series. From the set of preselected climate variables, we identify those CIDs that are most influential on the discharge quantities of selected return periods. Lastly, a filtering step is applied to go from influential to relevant CIDs by checking for plausibility.

2.3.1 GCM spread of initial variables of interest

The first step is to define potential CIDs that should be investigated and quantify the change factors in those variables. Often used climate variables in decision-scaling studies are yearly changes in average temperature, mean precipitation and the coefficient of variation (CV) of precipitation (El Garroussi et al., 2024; Fronzek et al., 2022; Ray et al., 2019; Taner et al., 2017; Steinschneider, McCrary, et al., 2015). These three variables are considered 'core variables' as these influence a broad array of climate-related flood processes (e.g. antecedent snowfall and melt, precipitation intensities, and soil moisture conditions). In the Lielupe basin, changing annual averages misrepresent future dynamics of extreme discharges since precipitation patterns change differently across the seasons in large parts of Europe (Gutiérrez et al., 2021). See also the specific dynamics of seasonal changes for the Lielupe basin in Figure A.3. Therefore, the study examines the impact relevance of the often used features in a seasonal manner. The seasons are defined as: winter (December-January-February), spring (March-April-May), summer (June-July-August) and autumn (September-October-November). Since temperature extremes scale similarly to temperature means (Seneviratne, et al., 2023), changes in temperature extremes relative to the mean seasonal changes are not considered.

To quantify the changes in these variables, we calculate the relative change of these seasonal features to the average value between 1940 and 2014 against the selected timeframes. The historical range of 1940-2014 has been selected since 2014 is the last year of many historical GCM simulations, and 1940 is the earliest year of ERA5 reanalysis data, later used to create future weather time series.

Using the dataset on CMIP6 climate projections from the Copernicus Climate Data Store (Copernicus Climate Change Service, 2021), grids for the region of interest are extracted for each available model and the SSP1-2.6, SSP2-4.5, SSP3-7.0, and SSP5-8.5 emission experiments, each ascending in emissions (see Table D.1 for a list of used model projections). Given the relatively small contribution of emission scenarios to the total variance of precipitation response patterns across models (Hawkins & Sutton, 2011; Lehner et al., 2020) we consider the selection of four emission scenarios sufficient to capture a large set of potential futures.

From the datasets, the average monthly near-surface air temperature is obtained together with daily accumulation values for precipitation amounts. The extracted data is masked by the identified climate region in Section 2.2. The relative change of a climate feature is found by comparing the feature value of a model, emission experiment and timeframe combination to the feature value of a model's historical run. Long-term area average seasonal temperature and precipitation sums were estimated (see Eq. 1 and Eq. 2). Then, seasonal changes in precipitation variability are defined by using the coefficient of variation (CV), which is a measure comparing the standard deviation of rainfall to the mean rainfall. The change in CV value is found by fitting a gamma distribution using the method of moments estimation for wet day (> 0.1 mm) rainfall time series per grid cell using the SciPy Python package (Virtanen et al., 2020) and obtaining the distribution's shape and scale parameters of . The CV value per cell is calculated by taking the inverse root of the fitted shape parameter. After finding grid cell CVs are averaging across the basin, we compare regional historic CV against regional scenario CV (See Eq. 3). Method of moments estimation is chosen as this better represents extremes in the mid-latitudes (Watterson, 2005; Watterson & Dix, 2003) which is of interest in this flood study. Gamma distributions have been shown to provide good estimations of daily rainfall probability density curves and for analysing changes in precipitation extremes and distributions under changing climate conditions (Martinez-Villalobos et al., 2022; Martinez-Villalobos & Neelin, 2019; Shadmehri Toosi et al., 2020; Watterson, 2005; Watterson & Dix, 2003; Wilby & Wigley, 2002).

$$\Delta P_{season} = \frac{\sum_{i=0}^{n} P_{i,season}^{projection}}{\sum_{i=0}^{n} P_{i,season}^{hisorical}} \qquad \text{(Eq. 1)}$$

Where:

ΔP_{season}: change factor in precipitation for a specific season [-]

P_{season}: precipitation averages in a season [mm/day]

i: specific cell [-]

n: total number of cells in data [-]

historical: data coming from the historical run of a GCM

projection: data coming from the projection run of a GCM

$$\Delta T_{season} = \frac{1}{n}\sum_{i=0}^{n} T_{i,season}^{projection} - \frac{1}{n}\sum_{i=0}^{n} T_{i,season}^{historical} \qquad \text{(Eq. 2)}$$

Where:

ΔT_{season}: temperature change for a specific seasons [°C]

T_{season}: average temperature in season [°C]

i: specific cell [-]

n: total number of cells in data [-]

historical: data coming from the historical run of a GCM

projection: data coming from the projection run of a GCM

$$\Delta CV_{season} = \frac{\frac{1}{n}\sum_{i=0}^{n} CV_{i,season}^{projection}}{\frac{1}{n}\sum_{i=0}^{n} CV_{i,seasom}^{historical}} = \frac{\frac{1}{n}\sum_{i=0}^{n} \frac{1}{\sqrt{k_{fitted,i,}^{projection}}}}{\frac{1}{n}\sum_{i=0}^{n} \frac{1}{\sqrt{k_{fitted,i}^{historical}}}} \qquad \text{(Eq. 3)}$$

Where:

CV: coefficient of variation [-]

ΔCV_{season}: change factor in coefficient of variation for a specific season [-]

i: specific cell [-]

n: total number of cells in data [-]

k_{fitted}: shape parameter of the fitted gamma function [-]

historical: data coming from the historical run of a GCM

projection: data coming from the projection run of a GCM

2.3.2 Future weather time series

Next, we apply a decision-scaling approach where the change factors across the GCM projections inform a stochastic weather generator (Brown et al., 2012). With stochastic weather generators, an extensive range of weather scenarios can be produced to identify climate vulnerability regimes for floods (Alcantara & Ahn, 2021; Steinschneider, Wi, et al., 2015). The approach entails a stochastic vulnerability analysis and, afterwards, performing a plausibility check using the collection of GCM projections. The weather generator is a key component of the study, and it allows the creation of high-resolution time series with a consistent sequence of events across different climate futures. High resolution is vital for meaningful hydrological modelling of discharge extremes in the region, and a consistent sequence of events is essential to analyse and compare the effect of changes in CIDs signalled by GCM projections. These requirements are lacking in available gridded GCM time series.

Using the weather generator as described by Steinschneider & Brown (2013), a synthetic baseline weather time series is made based on observed, historical, climate time series. Then, this time series is adjusted for future climates. In this case, we adjust the average seasonal temperature by adding an absolute degree change factor on top of the baseline climate realisation. For precipitation changes, a quantile mapping procedure is applied where the mean and CV of the baseline rainfall time series are adjusted to match future climate projections. Increasing the CV entails that small rainfall events will be smaller, and heavy rainfall events will be heavier. For a a detailed analysis of the synthetic baseline and application of the climate signals on this baseline, see Appendix B, and Steinschneider & Brown (2013)).

ERA5 reanalysis of 0.25x0.25° resolution from 1940-2014 (Hersbach et al., 2023) in the basin is used on a daily temporal resolution as input for the stochastic weather generator. The year 1940 is the earliest data available in the dataset and is chosen to be able to capture a large number of weather patterns to inform the stochastic weather generator. The year 2014 is selected to be able to compare it to historical runs of GCMs, which typically end then. Using the stochastic weather generator with historical information, a baseline synthetic weather time series of 100 years is created adhering to historical statistics (see Appendix B for statistics on the accuracy of historical climate pattern replication). The combinations of change factors to tweak the baseline time series are determined by sampling four values for each uncertain climate feature (ΔP, ΔCV, ΔT) in a season. The samples span the minimum to the maximum projected changes in the region with equal spacing. Within a season, each of these values is combined with the other values, leading to 4x4x4=64 scenarios per season and 256 in total. Each of these scenarios alters the synthetic baseline weather time series and is run in the hydrological model to obtain discharge extremes.

2.3.3 Assessing changes in discharge extremes

Discharge extremes are determined based on the annual maxima. Each annual maxima is coupled to a return period by dividing the number of years by the count of annual maxima that exceed or equal the specific annual maximum. The flows with a return period (RP) of 20, 50 and 100 years for each climate scenario are compared to the simulated extended historical climate time series. The comparison leads to a relative change from the current-day flows.

2.3.4 Importance and filtering of climate features

Not all climate features considered are necessarily influential on the discharge extremes. To find the climate variables that are most influential in changes on the impact, the Extra-Trees feature scoring algorithm (Geurts et al., 2006) is applied. This sensitivity analysis method links the seasonal climate features to the discharge variables. Higher feature scores of a climate

feature on an impact metric indicate a higher importance of that climate variable on the outcome. We apply the feature scoring algorithm implemented in the Python package EMAworkbench (Kwakkel, 2017).

After obtaining the climate feature importance, we select the two highest-ranking CIDs per impact metric. These are used to create impact-relevant climate scenarios. However, before final selection, the CIDs are subjected to a relevancy test. Relevancy is defined as a combination of high feature importance and plausibility when compared to GCM projections. We do this by plotting an impact response surface for the season and plotting projected changes of GCMs for each available timeframe and emission experiment. The impact response surface shows the discharge change under a combination of the two CIDs. If impact changes only occur at feature combinations that do not occur in the range of GCM projections, the impacts are not considered plausible, and then the variable is discarded and replaced with the subsequent CID that has the highest feature score.

2.4 Clustering GCM projections on relevant climate features

To identify new impact-oriented model clusters, a k-means clustering algorithm (Likas et al., 2003) is used to cluster model projections in a particular timeframe on the complete number (n) of selected climate features relevant to flood risk, represented by the impact metrics (RP20, RP50, RP100). The clustering of the models occurs in an n-dimensional space. The clustering optimises on two goals. Goal one is to keep data points within each cluster similar to each other. Goal two is to create clusters that are very different from each other. Separation of GCMs aids the selection of well-chosen scenarios that highlight the potential vulnerabilities, as discussed by Shepherd (2019). The number of clusters used is similar to the number of SSPs used (4) to compare the exploratory power of both methods with the same number of data points. The k-means algorithm is implemented using Python package scikit-learn (Boisberranger et al., 2024). The step results in clusters of models that exhibit similar behaviour for the targeted CIDs and the model means across all seasonal climate variables of those clusters to represent the climate signal throughout the year.

2.5 Comparing exploratory power

As a final step, the exploratory power of both methods is analysed and compared. Here, we define exploratory power as the ability to represent a range of impact values. For each scenario method, the range between the lowest impact model mean and the highest impact model mean is determined. The impact value is deduced from the impact response surface for the impact of interest. The impact response surfaces are created by running the hydrological model with 16 new weather time series that capture the interaction between chosen CIDs per impact metric. After obtaining the flow changes on a 4x4 grid, the grid is interpolated to identify flow changes inbetween grid points. Then, we compare the exploratory powers to find the exploratory amplification of the impact-oriented scenario method as in Eq. 4. A value below one means that the exploratory power is smaller than the emission-based method. A value above one means that the impact-oriented scenario method has higher exploratory power than the emission-based method.

$$EA = \frac{max(I_{SSP}) - min(I_{SSP})}{max(I_{Cluster}) - min(I_{Cluster})}$$

Eq. 4

Where:

EA = Exploratory Amplification [-]

I_{SSP} = Set of discharge change values for SSP means [%]

$I_{Cluster}$ = Set of discharge change values for cluster means [%]

3. Results

3.1 Climate region of interest

Following the steps described in section 2.2, we find the correlation areas for both precipitation and temperature as shown in in Figure 3. The correlated area of precipitation is smaller than that of temperature, and, therefore, the climate region of interest is defined as the non-white area describing the correlated precipitation area. Also, a clear non-correlation is seen in areas above water, even within the bounding box encompassing the correlated region.
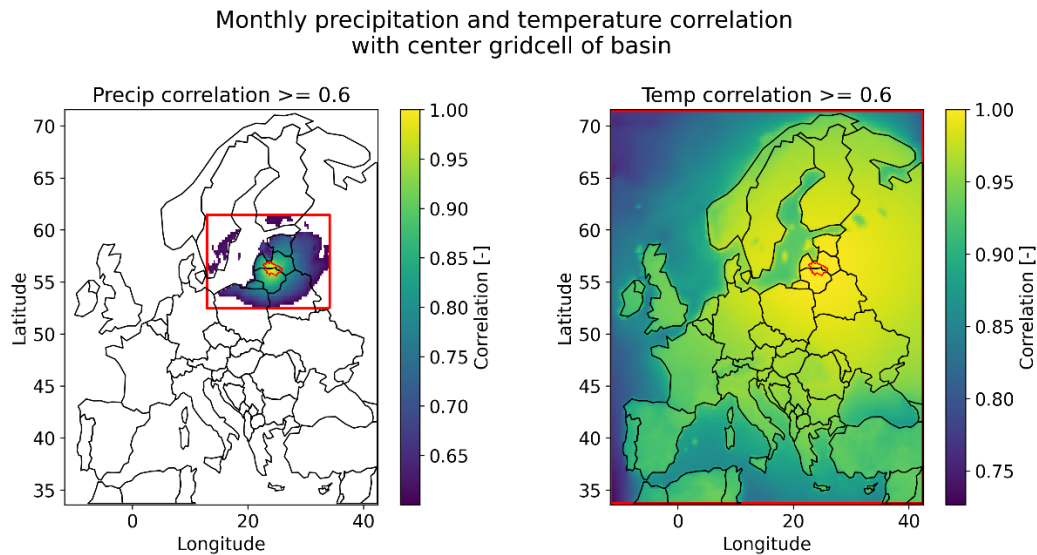
Figure 3: Correlation of monthly averaged precipitation (top) and temperature (bottom) time series of each grid cell when compared to the time series of the grid cell at the centre of the Lielupe basin. The heatmap shows the correlation value. The red square indicates the rectangular boundary of the region where the correlation condition is met, and the red shape indicates the boundary of the Lielupe basin. Country borders are shown in black.

3.2 Identify relevant climate features

After following the steps described in the methods, Table 1 shows how the analysed climate features influence the analysed impact metrics (RP20, RP50, RP100), representing the flood risk in the region.. For 100-year discharge, changes in the CV of precipitation during the spring season are most influential. High-scoring features in this season are expected since current-day high flows occur in spring. At a 50-year return period, mean precipitation and temperature changes in winter and mean precipitation in summer are important variables. In general, we find that high discharges occur when high rainfall amounts fall on saturated soil. At a 100-year discharge, the soil is already saturated before a large rainfall event (see Figure C.1 and Figure C.2), whereas for the other return period events, the soil is not pre-saturated, making average rainfall a more important factor of importance (see Figure C.3 and Figure C.4). Since current-day high-intensity rainfall occurs in summer but soil saturation is at its lowest, added average rainfall can greatly increase discharges. Next to this mechanism, we find that winter temperatures can also lead to high discharges when large quantities of snow start to melt at once. By a combination of low temperature change and increased mean precipitation in winter, more snow can accumulate during precipitation events and melt at once later in time, causing high river discharge. With increasing temperatures, more precipitation falls as rain, resulting in more uniform, and lower peak, discharges (see Figure C.5). For 50-year discharges to be governed by this mechanism, mean precipitation needs to increase while temperatures should not increase much (See Figure 4).

Table 1: Climate feature importance table on the impact indicators. The seasonal climate features are indicated for December-January-February (DJF), March-April-May (MAM), June-July-August (JJA), and September-October-November (SON). For each season, the influence of changes in average precipitation (ΔP), coefficient of variation (ΔCV) of that precipitation, and temperature (ΔT) on high discharges are shown. The impact metrics indicated by discharges with a return period (RP) of 20, 50 and 100 years are shown. Higher values indicate higher importance of a climate feature for the outcome of the impact metric. Features indicated with a "*" are used in the clustering of GCMs.

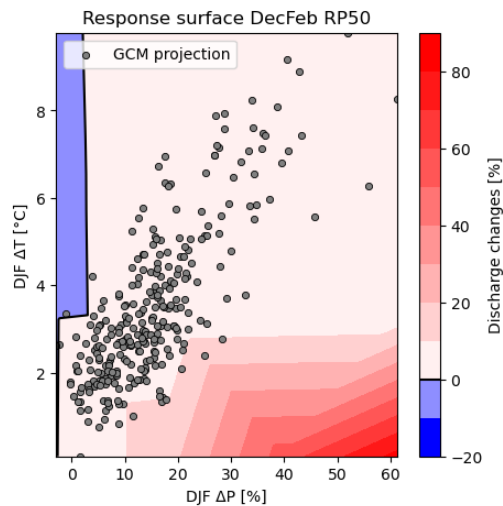| | | Impact Metrics | | |
		RP20	RP50	RP100
	ΔP	0.12	0.18	0.02
DJF	ΔCV	0.03	0.03	0.00
	ΔT	0.14	0.24	0.00
	ΔP	0.05	0.08*	0.07*
MAM	ΔCV	0.00	0.05	0.83*
	ΔT	0.01	0.01	0.07
	ΔP	0.30*	0.24*	0.00
JJA	ΔCV	0.05	0.06	0.00
	ΔT	0.03	0.03	0.00
	ΔP	0.18*	0.05	0.00
SON	ΔCV	0.08	0.03	0.00
	ΔT	0.01	0.01	0.00

Figure 4: Impact response surface plot showing the effect of change in average temperature during December-January-February (DJF ΔT) and average precipitation changes during the same months (DJF ΔP) on percentual changes of the 50-year return period discharge (indicated by the blue to red background hue). Each point represents a GCM model projection in the set that covers the 2021-2040, 2041-2060 and 2081-2100 periods in SSP126, SSP245, SSP370 and SSP585.

After analysing the two highest-scoring climate features per impact metric for plausibility, we find that 50-year discharge increases due to winter temperature changes are not plausible. None of the GCMs project conditions in which discharges change much (see Figure 4). Although the CIDs are influential, they are not considered relevant to the study area. For RP50, the two most relevant climate features are, therefore, mean changes in spring and summer precipitation. For RP20, autumn and summer precipitation means are most relevant. For RP100 we select CV changes in Spring. Since temperatures and mean precipitation

score equally high, we additionally choose mean spring precipitation since it is already in the set of relevant climate features and keeps complexity for clustering lower.

3.3 Clustering GCM projections on relevant climate features

Per timeframe, we clustered the set of GCM projections on the four most relevant climate features that alter flood risk across the various return periods, as found in the previous section. Here, we further examine the clusters created for the mid-century timeframe. For the mid-century, the four clusters can be characterised by the plots in **Error! Reference source not found.**. The plots show the mean of each cluster together with individual, cluster assigned, GCM projections to highlight the spread of each cluster for seasonal climate features. When considering the CIDs we clustered on, cluster one has a large change in rainfall variability during the spring period. As one of the main drivers for RP100 flows, this causes the flood risk to increase. The other precipitation impact drivers also increase, causing this cluster to have increased flows for all return periods. Cluster two projects decreases in the CV value in spring – lowering the RP100 flood risk. Cluster three is characterised by large changes in spring average rainfall, preconditioning wet soils and, therefore, increasing the 50-year flood discharge in spring. However, the model cluster's CV value in spring decreases and, therefore, lowers RP100 flows. Cluster four stands out by the decreases in summer rainfall limiting RP50 flow changes and decreasing RP20 flows.
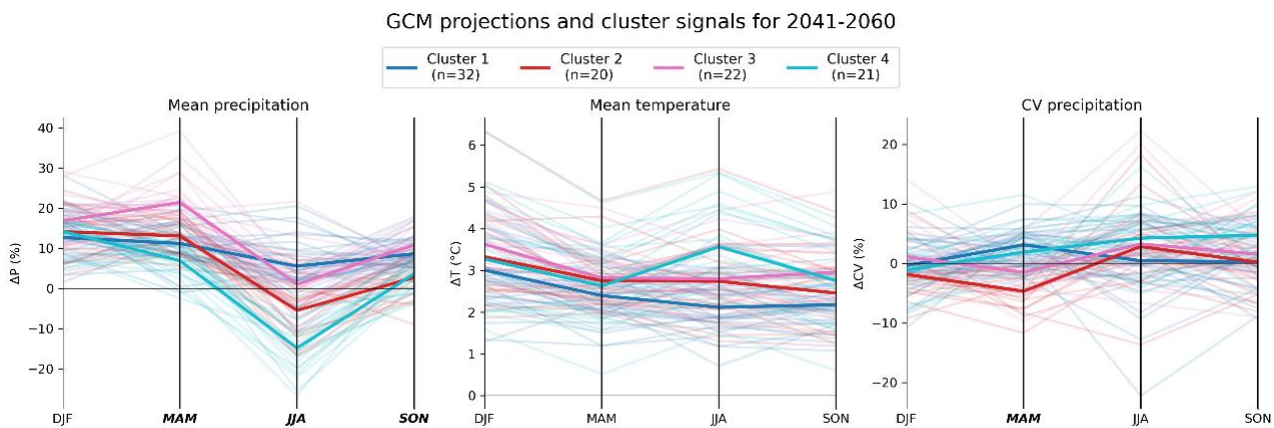

Figure 5: Parallel coordinates plot of clustered climate projections. Seasonal changes of individual GCM projection and cluster means are shown for precipitation averages (ΔP) and coefficient of variation (ΔCV) of that precipitation, and mean temperature changes (ΔT). Thick horizontal lines represent cluster means, while thin lines represent a single General Circulation Model (GCM) projection, colour-coded based on their assigned cluster. Seasonal changes for December-January-February (DJF), March-April-May (MAM), June-July-August (JJA), and September-October-November (SON) are given. The legend highlights the number of GCM projections in each model cluster. Variables used to cluster models are indicated in bold.

Variations in the clusters are thought to result from uncertainties in physical processes across climate models. Precipitation in Latvia is mainly governed by incoming westerly winds transporting moist air from the Atlantic Ocean which is influenced by large scale circulation patterns. In winter, the North Atlantic Oscillation (NAO) is a dominant factor bringing in precipitation (Jaagus et al., 2010; Klavins & Rodinov, 2010; Rutgersson et al., 2015). The NAO north-south position is also important (Rutgersson et al., 2015), although the pattern weakens in spring and only picks up again in autumn. In the transition seasons, meridional circulation patterns, such as the Scandinavian blocking pattern, are a large determinant of precipitation amounts (Klavins & Rodinov, 2010). However, large uncertainties exist in changes of the strength of the NAO, the position of the NAO and blocking frequencies across models due to different weights given to different physical processes and potentially missing dynamical processes (Doblas-Reyes et al., 2023; Douville et al., 2023; Lee et al., 2023; Ranasinghe et al., 2023). One such mechanism is the interaction between the Atlantic Meridional Overturning Circulation and the atmosphere, which in turn influences precipitation patterns in Europe (Börgel et al., 2022, 2023).

It has been found that these circulation patterns can be key drivers of local expressions of the mean climate (van den Hurk et al., 2014). For our case changes in circulation can alter the mean climate in the following ways.that A strong NAO causes the jet stream to extend more towards eastern Europe and brings more precipitation; a shift of the westerlies northward also brings more moist air, while a southward shift brings more cold and dry air from the polar region. More blocking over the region results in moist air from the ocean being blocked and, therefore, less precipitation in the area. High increases in average precipitation can, therefore, mean two things. One is that there is less frequent blocking and, therefore, more uniform precipitation coming from a strengthened NAO and in a more northward position over Latvia. Or, the blocking frequencies

increase due to a weakening of the NAO, and when it does rain, it pours heavily. Lower increases in average precipitation can indicate a weakening of the NAO or NAO position that is more southward, bringing in less moist air. An increase in blocking can also keep the moist westerlies out, resulting in lower average precipitation. These are physical reasons why various clusters can be derived as each cluster can have a combination of these precipitation drivers. However, the complex interaction of smaller drivers cannot be excluded from the overall resulting changes.

3.4 Comparing exploratory power

Using the new clusters of GCMs, we analyse the exploratory power of the impact-oriented cluster means and emission-based model means for the mid-century. In Figure 6, both emission-based and impact-oriented cluster means are plotted on an impact response surface to deduce the impact values for both sets of means and individual GCM projections. These impact values can be visualised in Figure 7, showing the various impact values. We can see that the range of individual GCM projections can be much larger the mean values of both SSP means and cluster means. Furthermore, we notice that various SSP projection scenarios can fall into the same cluster category. These individual projections might belong to different emission scenarios but result in similar expressions of climatic change in regional CIDs. Lastly, we note that the exploratory range for all discharge return periods is larger for the cluster means than the SSP means. We compare these ranges to obtain the exploratory amplification. Overall, the exploratory amplification increases for all return periods. For the 20-year return period, the exploratory amplification is the smallest, with 3.2 times the exploratory power of emission-based means, whereas the return period of 100 years has the largest amplification factor of 8.7. This can be partly explained by the fact that the climate feature governing the 100-year return period has a very clear feature importance. For the 20- and 50-year return period, the relevancy is more spread out across the initial set of climate features.It is, therefore, tougher to get a clear impact signal from just the two most relevant CIDs.

Table 2 shows the development of the projections for RP50 over the various timeframes. Noticeable in the table is that the exploratory amplification factor decreases when considering timeframes further into the future. One reason is that over time the climate response due to emissions becomes clearer over time as the inertia of the climate system is overcome and the role of internal variability becomes smaller (Samset et al., 2020; Tebaldi & Friedlingstein, 2013). Therefore, the emission-based model means start to diverge over time, and the explored impact will, therefore, increase. It must be noted that the explored impact range of impact-oriented model means is still 2.7x that of emissions-based model means.

Table 2: Exploratory amplification numbers of the impact relevant cluster means versus emission-based model means for the different impact metrics and timeframes.

		Timeframe		
		2021-2040	*2041-2060*	*2081-2100*
Impact metric	*RP20*	4.82	3.21	2.65
	RP50	7.68	6.04	6.57
	RP100	9.4	8.74	5.94

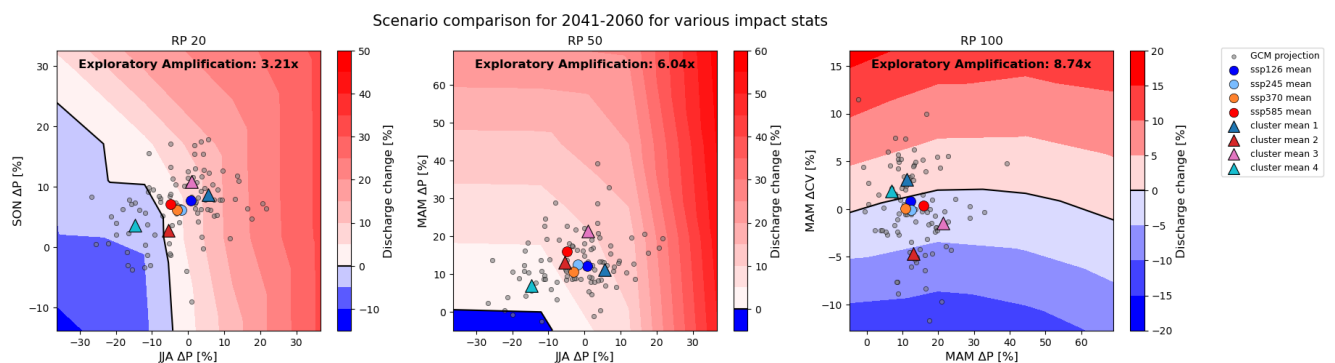Scenario comparison for 2041-2060 for various impact stats

Figure 6: Impact response for the 2041-2060 timeframe for the different impact variables of interest and their top two climate features of importance. Where the axis labels represent seasonal changes for March-April-May (MAM), June-July-August (JJA), and September-October-November (SON). For selected seasons, the changes in average precipitation (ΔP) and coefficient of variation (ΔCV) of that precipitation are shown. The background hue indicates the discharge increase for that return period at any combination of the selected climate features. Each grey point represents an individual GCM model projection for SSP126, SSP245, SSP370 and SSP585. The coloured circles represent the SSP model means, and coloured triangles represent the impact-oriented model means of the different clusters. The exploratory amplification for each return period is given below each plot.
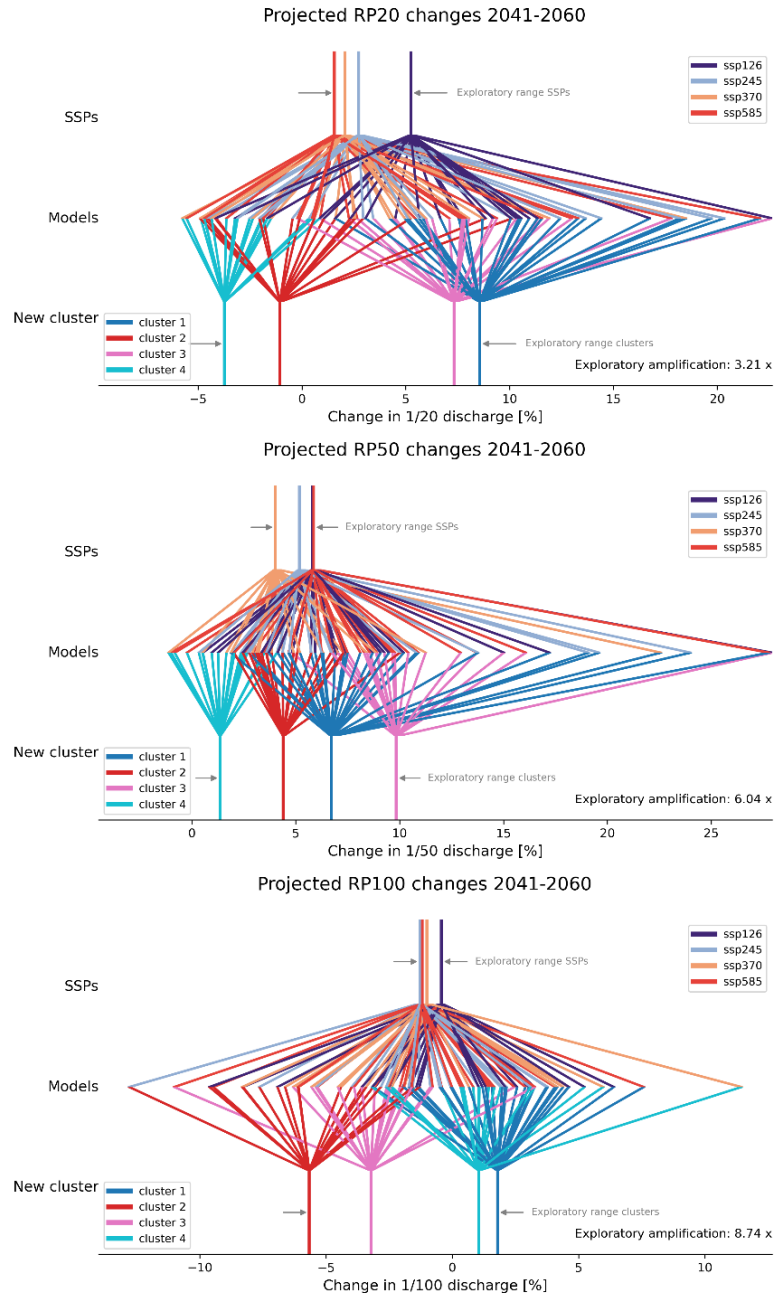
Figure 7: Projected changes in river discharges for 20, 50, and 100-year return periods (RP) based on SSP model means, individual GCM projections and cluster means for the mid-century (2041-2060). Each plot displays SSP projection means in the top section, these are disaggregated into individual GCM projections in the middle section. These GCM projections are placed into specific clusters, and averaged to provide the corresponding cluster means at the bottom section of each plot. The exploratory range of each method is marked by the distance between the arrows. These can be compared to investigate the exploratory amplification of the new method versus the SSPs model mean method.

4. Discussion

In this paper, we introduced a procedure to enhance the exploratory power of future climate scenarios by clustering projections based on locally relevant climatic impact drivers instead of emission-based model means. A comprehensive exploration of the future risk range is needed to aid decisions today to adapt to an uncertain climate future tomorrow. We illustrated the procedure's effectiveness by applying the framework to a riverine flood study for the Lielupe basin in Latvia. For the mid-century, the explored impact range can increase by a factor of 3.2 to 8.7. Also, the different scenario clusters reveal that the high discharge with a 20 and 100-year return probability can either increase or decrease depending on particular climate response features. This largely depends on uncertainties in the response of large-scale earth system processes, such as the NAO, blocking patterns, and AMOC to changing emission concentrations (Börgel et al., 2022; Doblas-Reyes et al., 2023; Douville et al., 2023; Lee et al., 2023; Ranasinghe et al., 2023). A set of climate scenarios created using our approach could aid the adaptation planning process by evaluating the robustness of potential measures across scenarios.

4.1 Impact driver-based clustering and earth system process clustering

In this study, we substantiate uncertainties in climatic impact drivers with uncertainties in earth system processes under a changing climate. In climate literature, there is a body of work on physically consistent storylines (Shepherd et al., 2018; Zappa & Shepherd, 2017) where the behaviour of large-scale physical processes such as tropical and polar amplification, polar vortex strength or AMOC stability of different GCMs are isolated to highlight the spread of future climate conditions (Bulgin et al., 2023; Zappa & Shepherd, 2017). The Dutch climate scenarios take such an approach where regionally relevant circulation patterns and their uncertain response to a warming climate are used to highlight the envelope of climate uncertainty (van den Hurk, 2022; van der Wiel et al., 2024). These types of scenarios allow a variety of domains to work with a consistent set of scenarios, which enhances cooperation across stakeholders due to a common basis.

However, these storylines are often created considering earth system processes that explain a large fraction of variability of set 'target variables'. These target variables may not reflect all sector-specific dominant impact features and thus prove to be sub-optimally. To create storylines that fit these needs, substantial knowledge is required about the relationship between locally relevant climatic impact drivers and large-scale climate processes. This includes understanding rare but (possibly significant) combinations of earth system interactions determining local impact. Disentangling many processes in separate scenarios leads to an unfeasible number of scenarios, overrunning the decision-maker's capacity.

Our method does not identify specific earth system processes driving local variability but does acknowledge their existence and contribution to uncertainty in the CIDs. System knowledge from local users on which CIDs are most relevant for local impacts is helpful to optimise a scenario framework also without detailed a priori knowledge on key driving large-scale earth system processes. This system knowledge is often available through local stakeholders (New et al., 2023)

In summary, physical storylines have their merits in providing a solid scientific basis of uncertainties and how they affect future climate. Tailoring these storylines to local conditions enhances their specificity and applicability for sectoral planning.

4.2 Framework opportunities and limitations

Although this study illustrates a riverine flood study, the proposed procedure is generic and can be implemented for any river basin of interest, provided the availability of adequate climate data and a hydrological modelling capability. The framework itself is flexible and can be adjusted to incorporate regional models, alternative risk metrics, and climate features of interest. This increases the framework's applicability to the local scale and trust in the outcomes. This study used a data and modelling-intensive method to find relevant CIDs. However, one can also directly identify these climate features using local knowledge and extract the CID values from GCM projections. The framework can be extended to other hazards where emission-based model means do not necessarily have a large exploratory power for future impacts. Since the climate response of rainfall is uncertain in many areas of the world (Douville et al., 2023), particularly for mid-century conditions with little contrast between multi-model mean responses to different emission scenarios (Hawkins & Sutton, 2011; Lehner et al., 2020), most water-driven hazards (not only floods, but also droughts or fire weather conditions) are good candidates. The proposed methodology allows for a multi-hazard scenario selection, but relevant CIDs for all hazards and fitting impact metrics should be considered and included in the process.

A few limitations apply to the framework. The procedure does not explicitly distinguish between internal variability and forced climate response. The combination of these highlights the total range of future risks. The forced response can be isolated by the application of 'single-model initial-condition large ensembles' (SMILEs), designed to separate internal variability and the forced climate response (Maher et al., 2021). Furthermore, the study only used changes in CIDs using GCM runs driven by SSP scenarios. The socio-economic dimension of these scenarios (O'Neill et al., 2017) is not explicitly sampled in our approach. Considering risk to be a combination of hazard, exposure, vulnerability (Field et al., 2014), and response (Simpson et al., 2021),

expansion of the framework representing relevant socio-economic impact drivers may improve the assessment of changes in regional risk profiles.

The choice of climate variables to define the relevant CIDs in this study is partly restricted by the capabilities of the weather generator and computational resources, which limited the number of alternative realisations of time series from the weather generator. Due to sampling uncertainty in stochastic weather generators (Alodah & Seidou, 2020) the resulting return probabilities of given intensities may depend on the number of time series samples. This affects the assessment of the impact range amplification achieved by our methodology.

This study uses CMIP6 model outcomes without any selection or screening. However, not all models are suitable for every analysis and every region, and there are many ways to assess this (Raju & Kumar, 2020). The proposed framework allows for filtering input models when the filter specifications are defined. Higher resolution results may be achieved by using slightly older, but bias corrected CMIP5 based CORDEX data (Giorgi & Gutowski, 2015) or once available CMIP6-based CORDEX data. These data may be more suitable for regional analysis.

5. Conclusion

Future climate projections across global climate models show a large range of potential futures due to internal variability and varying model representations of physical processes and their response to emissions. Taking multi-model means of the emission scenarios, one loses vital information on the potential risk indicated by individual models. Separating models into multiple clusters can help gain insight into a broad range of climate risks that occur due to various underlying earth system processes. Here, we presented and illustrated a framework where locally relevant climatic impact drivers are used to cluster projections, and this allows us to explore up to eight times the impact range when compared to using multi-model means of emission scenarios. Not only is the range extended, but we also found that risk can increase or decrease depending on the selected cluster. The framework helps the analysis of future impacts while aggregating a large sample of model projections into an affordable set of scenarios to explore. Overall, the framework allows for an enhanced exploration of future climate risks to aid adaptation decision-making.

Acknowledgements

Data availability statement
The CMIP6 data can be freely obtained through https://cds.climate.copernicus.eu/cdsapp#!/dataset/projections-cmip6. The historical ERA5 data is obtained from https://cds.climate.copernicus.eu/cdsapp#!/dataset/reanalysis-era5-pressure-levels. Implementation of the used weather generator can be found at https://github.com/Deltares-research/weathergenr. Analysis code and data used in this study is published at Zenodo (https://doi.org/10.5281/zenodo.11638284) and on Github (https://github.com/TBuskop/Enhancing-impact-exploration)

References

Alcantara, A. L., & Ahn, K.-H. (2021). Future flood riverine risk analysis considering the heterogeneous impacts

from tropical cyclone and non-tropical cyclone rainfalls: Application to daily flows in the Nam River

Basin, South Korea. *Advances in Water Resources*, *154*, 103983.

https://doi.org/10.1016/j.advwatres.2021.103983

Alodah, A., & Seidou, O. (2020). Influence of output size of stochastic weather generators on common climate and hydrological statistical indices. *Stochastic Environmental Research and Risk Assessment*, *34*(7), 993–1021. Scopus. https://doi.org/10.1007/s00477-020-01825-w

Bankes, S. (1993). Exploratory Modeling for Policy Analysis. *Operations Research*, *41*(3), 435–449. https://doi.org/10.1287/opre.41.3.435

Bankes, S., Walker, W. E., & Kwakkel, J. H. (2013). Exploratory Modeling and Analysis. In S. I. Gass & M. C. Fu (Eds.), *Encyclopedia of Operations Research and Management Science* (pp. 532–537). Springer US. https://doi.org/10.1007/978-1-4419-1153-7_314

Bednar-Friedl, B., Biesbroek, R., Schmidt, D. N., Alexander, P., Børsheim, K. Y., Carnicer, J., Georgopoulou, E., Haasnoot, M., Le Cozannet, G., Lionello, P., Lipka, O., Möllmann, C., Muccione, V., Mustonen, T., Piepenburg, D., & Whitmarsh, L. (2022). Europe. In H.-O. Pörtner, D. C. Roberts, M. M. B. Tignor, E. S. Poloczanska, K. Mintenbeck, A. Alegría, M. Craig, S. Langsdorf, S. Löschke, V. Möller, A. Okem, & B. Rama (Eds.), *Climate Change 2022: Impacts, Adaptation and Vulnerability. Contribution of Working Group II to the Sixth Assessment Report of the Intergovernmental Panel on Climate Change*. Cambridge University Press. https://www.ipcc.ch/report/ar6/wg2/downloads/report/IPCC_AR6_WGII_Chapter13.pdf

Blankespoor, B., Dasgupta, S., Wheeler, D., Jeuken, A., van Ginkel, K., Hill, K., & Hirschfeld, D. (2023). Linking sea-level research with local planning and adaptation needs. *Nature Climate Change*, *13*(8), Article 8. https://doi.org/10.1038/s41558-023-01749-7

Boisberranger, J. du, Bossche, J. V. den, Estève, L., Fan, T. J., Gramfort, A., Grisel, O., Halchenko, Y., Head, T., Hug, N., Jalali, A., Jerphanion, J., Lemaitre, G., Lorentzen, C., Metzen, J. H., Mueller, A., Niculae, V., Nothman, J., Qin, H., Salman, O., … Meekail Zain. (2024). *Scikit-learn: Machine learning in Python—Scikit-learn 1.5.2 documentation*. https://scikit-learn.org/stable/index.html

Börgel, F., Gröger, M., Meier, H. E. M., Dutheil, C., Radtke, H., & Borchert, L. (2023). The impact of Atlantic Multidecadal Variability on Baltic Sea temperatures limited to winter. *Npj Climate and Atmospheric Science*, *6*(1), 1–9. https://doi.org/10.1038/s41612-023-00373-8

Börgel, F., Meier, H. E. M., Gröger, M., Rhein, M., Dutheil, C., & Kaiser, J. M. (2022). Atlantic multidecadal

variability and the implications for North European precipitation. *Environmental Research Letters*, *17*(4),

044040. https://doi.org/10.1088/1748-9326/ac5ca1

Brown, C., Ghile, Y., Laverty, M., & Li, K. (2012). Decision scaling: Linking bottom-up vulnerability analysis with

climate projections in the water sector. *Water Resources Research*, *48*(9), 2011WR011212.

https://doi.org/10.1029/2011WR011212

Bulgin, C. E., Mecking, J. V., Harvey, B. J., Jevrejeva, S., McCarroll, N. F., Merchant, C. J., & Sinha, B. (2023).

Dynamic sea-level changes and potential implications for storm surges in the UK: A storylines

perspective. *Environmental Research Letters*, *18*(4), 044033. https://doi.org/10.1088/1748-9326/acc6df

Cook, B. I., Mankin, J. S., Marvel, K., Williams, A. P., Smerdon, J. E., & Anchukaitis, K. J. (2020). Twenty-First

Century Drought Projections in the CMIP6 Forcing Scenarios. *Earth's Future*, *8*(6), e2019EF001461.

https://doi.org/10.1029/2019EF001461

Copernicus Climate Change Service. (2021). *CMIP6 predictions underpinning the C3S decadal prediction

prototypes* [Dataset]. ECMWF. https://doi.org/10.24381/CDS.C866074C

Doblas-Reyes, F. J., Sörensson, A. A., Almazroui, M., Dosio, A., Gutowski, W. J., Haarsma, R., Hamdi, R., Hewitson,

B., Kwon, W.-T., Lamptey, B. L., Maraun, D., Stephenson, T. S., Takayabu, I., Terray, L., Turner, A., & Zuo,

Z. (2023). Linking Global to Regional Climate Change. In *Climate Change 2021 – The Physical Science

Basis: Working Group I Contribution to the Sixth Assessment Report of the Intergovernmental Panel on

Climate Change* (pp. 1363–1512). Cambridge University Press.

https://doi.org/10.1017/9781009157896.012

Douville, H., Raghavan, K., Renwick, J., Allan, R. P., Arias, P. A., Barlow, M., Cerezo-Mota, R., Cherchi, A., Gan, T.

Y., Gergis, J., Jiang, D., Khan, A., Pokam Mba, W., Rosenfeld, D., Tierney, J., & Zolina, O. (2023). Water

Cycle Changes. In *Climate Change 2021 – The Physical Science Basis: Working Group I Contribution to the

Sixth Assessment Report of the Intergovernmental Panel on Climate Change* (pp. 1055–1210). Cambridge

University Press. https://doi.org/10.1017/9781009157896.010

Eilander, D., Boisgontier, H., Bouaziz, L. J. e, Buitink, J., Couasnon, A., Dalmijn, B., Hegnauer, M., Jong, T. de, Loos, S., Marth, I., & van Verseveld, W. (2023). HydroMT: Automated and reproducible model building and analysis. *Journal of Open Source Software*, *8*(83), 4897. https://doi.org/10.21105/joss.04897

El Garroussi, S., Di Giuseppe, F., Barnard, C., & Wetterhall, F. (2024). Europe faces up to tenfold increase in extreme fires in a warming climate. *Npj Climate and Atmospheric Science*, *7*(1), Article 1. https://doi.org/10.1038/s41612-024-00575-8

Field, C. B., Barros, V. R., Dokken, D. J., Mach, K. J., & Mastrandrea, M. D. (Eds.). (2014). *Climate Change 2014 Impacts, Adaptation, and Vulnerability: Working Group II Contribution to the Fifth Assessment Report of the Intergovernmental Panel on Climate Change*. Cambridge University Press. https://doi.org/10.1017/CBO9781107415379

Fronzek, S., Honda, Y., Ito, A., Nunes, J. P., Pirttioja, N., Räisänen, J., Takahashi, K., Terämä, E., Yoshikawa, M., & Carter, T. R. (2022). Estimating impact likelihoods from probabilistic projections of climate and socio-economic change using impact response surfaces. *Climate Risk Management*, *38*, 100466. https://doi.org/10.1016/j.crm.2022.100466

Geurts, P., Ernst, D., & Wehenkel, L. (2006). Extremely randomized trees. *Machine Learning*, *63*(1), 3–42. https://doi.org/10.1007/s10994-006-6226-1

Giorgi, F., & Gutowski, W. J. (2015). Regional Dynamical Downscaling and the CORDEX Initiative. *Annual Review of Environment and Resources*, *40*(1), 467–490. https://doi.org/10.1146/annurev-environ-102014-021217

Goulart, H. M. D., van der Wiel, K., Folberth, C., Balkovic, J., & van den Hurk, B. (2021). Storylines of weather-induced crop failure events under climate change. *Earth System Dynamics*, *12*(4), 1503–1527. https://doi.org/10.5194/esd-12-1503-2021

Gutiérrez, J. M., R.G. Jones, G.T. Narisma, L.M. Alves, M. Amjad, I.V. Gorodetskaya, M. Grose, N.A.B. Klutse, S. Krakovska, J. Li, D. Martínez-Castro, L.O. Mearns, S.H. Mernild, T. Ngo-Duc, B. van den Hurk, & J.-H. Yoon. (2021). Atlas. In *Climate Change 2021: The Physical Science Basis. Contribution of Working Group I*

to the Sixth Assessment Report of the Intergovernmental Panel on Climate Change (pp. 1927–2058). https://doi.org/10.1017/9781009157896.021

Hawkins, E., & Sutton, R. (2011). The potential to narrow uncertainty in projections of regional precipitation change. *Climate Dynamics*, *37*(1), 407–418. https://doi.org/10.1007/s00382-010-0810-6

Hersbach, H., Bell, B., Berrisford, P., Biavati, G., Horányi, A., Sabater, J. M., Nicolas, J., Peubey, C., Radu, R., Rozum, I., Schepers, D., Simmons, A., Soci, C., Dee, D., & Thépaut, J.-N. (2023). *ERA5 hourly data on pressure levels from 1940 to present* [Dataset]. Copernicus Climate Change Service (C3S) Climate Data Store (CDS). https://doi.org/10.24381/cds.bd0915c6

Jaagus, J., Briede, A., Rimkus, E., & Remm, K. (2010). Precipitation pattern in the Baltic countries under the influence of large-scale atmospheric circulation and local landscape factors. *International Journal of Climatology*, *30*(5), 705–720. https://doi.org/10.1002/joc.1929

Klavins, M., & Rodinov, V. (2010). Influence of large-scale atmospheric circulation on climate in Latvia. *Boreal Environment Research*, *15*(6), 533–543.

Kwakkel, J. H. (2017). The Exploratory Modeling Workbench: An open source toolkit for exploratory modeling, scenario discovery, and (multi-objective) robust decision making. *Environmental Modelling & Software*, *96*, 239–250. https://doi.org/10.1016/j.envsoft.2017.06.054

Lee, J.-Y., Marotzke, J., Bala, G., Cao, L., Corti, S., Dunne, J. P., Engelbrecht, F., Fischer, E., Fyfe, J. C., Jones, C., Maycock, A., Mutemi, J., Ndiaye, O., Panickal, S., & Zhou, T. (2023). Future Global Climate: Scenario-based Projections and Near-term Information. In *Climate Change 2021 – The Physical Science Basis: Working Group I Contribution to the Sixth Assessment Report of the Intergovernmental Panel on Climate Change* (pp. 553–672). Cambridge University Press. https://doi.org/10.1017/9781009157896.006

Lehner, F., Deser, C., Maher, N., Marotzke, J., Fischer, E. M., Brunner, L., Knutti, R., & Hawkins, E. (2020). Partitioning climate projection uncertainty with multiple large ensembles and CMIP5/6. *Earth System Dynamics*, *11*(2), 491–508. https://doi.org/10.5194/esd-11-491-2020

Likas, A., Vlassis, N., & J. Verbeek, J. (2003). The global *k*-means clustering algorithm. *Pattern Recognition*, *36*(2), 451–461. https://doi.org/10.1016/S0031-3203(02)00060-2

Maher, N., Power, S. B., & Marotzke, J. (2021). More accurate quantification of model-to-model agreement in externally forced climatic responses over the coming century. *Nature Communications*, *12*(1), 788. https://doi.org/10.1038/s41467-020-20635-w

Martinez-Villalobos, C., & Neelin, J. D. (2019). Why Do Precipitation Intensities Tend to Follow Gamma Distributions? *Journal of the Atmospheric Sciences*, *76*(11), 3611–3631. https://doi.org/10.1175/JAS-D-18-0343.1

Martinez-Villalobos, C., Neelin, J. D., & Pendergrass, A. G. (2022). Metrics for Evaluating CMIP6 Representation of Daily Precipitation Probability Distributions. *Journal of Climate*, *35*(17), 5719–5743. https://doi.org/10.1175/JCLI-D-21-0617.1

Measham, T. G., Preston, B. L., Smith, T. F., Brooke, C., Gorddard, R., Withycombe, G., & Morrison, C. (2011). Adapting to climate change through local municipal planning: Barriers and challenges. *Mitigation and Adaptation Strategies for Global Change*, *16*(8), 889–909. https://doi.org/10.1007/s11027-011-9301-2

Merz, B., Blöschl, G., Vorogushyn, S., Dottori, F., Aerts, J. C. J. H., Bates, P., Bertola, M., Kemter, M., Kreibich, H., Lall, U., & Macdonald, E. (2021). Causes, impacts and patterns of disastrous river floods. *Nature Reviews Earth & Environment*, *2*(9), 592–609. https://doi.org/10.1038/s43017-021-00195-3

Mora, C., Frazier, A. G., Longman, R. J., Dacks, R. S., Walton, M. M., Tong, E. J., Sanchez, J. J., Kaiser, L. R., Stender, Y. O., Anderson, J. M., Ambrosino, C. M., Fernandez-Silva, I., Giuseffi, L. M., & Giambelluca, T. W. (2013). The projected timing of climate departure from recent variability. *Nature*, *502*(7470), Article 7470. https://doi.org/10.1038/nature12540

New, M., D. Reckien, D. Viner, C. Adler, S.-M. Cheong, C. Conde, A. Constable, E. Coughlan de Perez, A. Lammel, R. Mechler, B. Orlove, & W. Solecki. (2023). Decision-Making Options for Managing Risk. In *Climate Change 2022 – Impacts, Adaptation and Vulnerability: Working Group II Contribution to the Sixth*

Assessment Report of the Intergovernmental Panel on Climate Change (pp. 2539–2654). Cambridge University Press. https://doi.org/10.1017/9781009325844.026

O'Neill, B. C., Kriegler, E., Ebi, K. L., Kemp-Benedict, E., Riahi, K., Rothman, D. S., van Ruijven, B. J., van Vuuren, D. P., Birkmann, J., Kok, K., Levy, M., & Solecki, W. (2017). The roads ahead: Narratives for shared socioeconomic pathways describing world futures in the 21st century. *Global Environmental Change*, *42*, 169–180. https://doi.org/10.1016/j.gloenvcha.2015.01.004

Raju, K. S., & Kumar, D. N. (2020). Review of approaches for selection and ensembling of GCMs. *Journal of Water and Climate Change*, *11*(3), 577–599. https://doi.org/10.2166/wcc.2020.128

Ranasinghe, R., Ruane, A. C., Vautard, R., Arnell, N., Coppola, E., Cruz, F. A., Dessai, S., Islam, A. S., Rahimi, M., Ruiz Carrascal, D., Sillmann, J., Sylla, M. B., Tebaldi, C., Wang, W., & Zaaboul, R. (2023). Climate Change Information for Regional Impact and for Risk Assessment. In *Climate Change 2021 – The Physical Science Basis: Working Group I Contribution to the Sixth Assessment Report of the Intergovernmental Panel on Climate Change* (pp. 1767–1926). Cambridge University Press. https://doi.org/10.1017/9781009157896.014

Ray, P. A., Taner, M. Ü., Schlef, K. E., Wi, S., Khan, H. F., Freeman, S. S. G., & Brown, C. M. (2019). Growth of the Decision Tree: Advances in Bottom-Up Climate Change Risk Management. *JAWRA Journal of the American Water Resources Association*, *55*(4), 920–937. https://doi.org/10.1111/1752-1688.12701

Rojas, R., Feyen, L., & Watkiss, P. (2013). Climate change and river floods in the European Union: Socio-economic consequences and the costs and benefits of adaptation. *Global Environmental Change*, *23*(6), 1737–1751. https://doi.org/10.1016/j.gloenvcha.2013.08.006

Ruane, A. C., Vautard, R., Ranasinghe, R., Sillmann, J., Coppola, E., Arnell, N., Cruz, F. A., Dessai, S., Iles, C. E., Islam, A. K. M. S., Jones, R. G., Rahimi, M., Carrascal, D. R., Seneviratne, S. I., Servonnat, J., Sörensson, A. A., Sylla, M. B., Tebaldi, C., Wang, W., & Zaaboul, R. (2022). The Climatic Impact-Driver Framework for Assessment of Risk-Relevant Climate Information. *Earth's Future*, *10*(11). https://doi.org/10.1029/2022EF002803

Rutgersson, A., Jaagus, J., Schenk, F., Stendel, M., Bärring, L., Briede, A., Claremar, B., Hanssen-Bauer, I.,

Holopainen, J., Moberg, A., Nordli, Ø., Rimkus, E., & Wibig, J. (2015). Recent Change—Atmosphere. In

The BACC II Author Team (Ed.), *Second Assessment of Climate Change for the Baltic Sea Basin* (pp. 69–

97). Springer International Publishing. https://doi.org/10.1007/978-3-319-16006-1_4

Samset, B. H., Fuglestvedt, J. S., & Lund, M. T. (2020). Delayed emergence of a global temperature response after

emission mitigation. *Nature Communications*, *11*(1), 3261. https://doi.org/10.1038/s41467-020-17001-1

Seneviratne, S. I., Zhang, X., Adnan, M., Badi, W., Dereczynski, C., Luca, A. D., Ghosh, S., Iskandar, I., Kossin, J.,

Lewis, S., Otto, F., Pinto, I., Satoh, M., Vicente-Serrano, S. M., Wehner, M., & Zhou, B. (2023). Weather

and Climate Extreme Events in a Changing Climate. In *Climate Change 2021 – The Physical Science Basis:*

Working Group I Contribution to the Sixth Assessment Report of the Intergovernmental Panel on Climate

Change (pp. 1513–1766). Cambridge University Press. https://doi.org/10.1017/9781009157896.013

Shadmehri Toosi, A., Doulabian, S., Ghasemi Tousi, E., Calbimonte, G. H., & Alaghmand, S. (2020). Large-scale

flood hazard assessment under climate change: A case study. *Ecological Engineering*, *147*, 105765.

https://doi.org/10.1016/j.ecoleng.2020.105765

Shepherd, T. G. (2019). Storyline approach to the construction of regional climate change information.

Proceedings of the Royal Society A: Mathematical, Physical and Engineering Sciences, *475*(2225),

20190013. https://doi.org/10.1098/rspa.2019.0013

Shepherd, T. G., Boyd, E., Calel, R. A., Chapman, S. C., Dessai, S., Dima-West, I. M., Fowler, H. J., James, R.,

Maraun, D., Martius, O., Senior, C. A., Sobel, A. H., Stainforth, D. A., Tett, S. F. B., Trenberth, K. E., van

den Hurk, B. J. J. M., Watkins, N. W., Wilby, R. L., & Zenghelis, D. A. (2018). Storylines: An alternative

approach to representing uncertainty in physical aspects of climate change. *Climatic Change*, *151*(3),

555–571. https://doi.org/10.1007/s10584-018-2317-9

Simpson, N. P., Mach, K. J., Constable, A., Hess, J., Hogarth, R., Howden, M., Lawrence, J., Lempert, R. J.,

Muccione, V., Mackey, B., New, M. G., O'Neill, B., Otto, F., Pörtner, H. O., Reisinger, A., Roberts, D.,

Schmidt, D. N., Seneviratne, S., Strongin, S., … Trisos, C. H. (2021). A framework for complex climate change risk assessment. *One Earth*, *4*(4), 489–501. https://doi.org/10.1016/J.ONEEAR.2021.03.005

Spence, C. M., & Brown, C. M. (2016). Nonstationary decision model for flood risk decision scaling. *Water Resources Research*, *52*(11), 8650–8667. Scopus. https://doi.org/10.1002/2016WR018981

Steinschneider, S., & Brown, C. (2013). A semiparametric multivariate, multisite weather generator with low-frequency variability for use in climate risk assessments. *Water Resources Research*, *49*(11), 7205–7220. https://doi.org/10.1002/wrcr.20528

Steinschneider, S., McCrary, R., Wi, S., Mulligan, K., Mearns, L. O., & Brown, C. (2015). Expanded Decision-Scaling Framework to Select Robust Long-Term Water-System Plans under Hydroclimatic Uncertainties. *Journal of Water Resources Planning and Management*, *141*(11), 04015023. https://doi.org/10.1061/(ASCE)WR.1943-5452.0000536

Steinschneider, S., Wi, S., & Brown, C. (2015). The integrated effects of climate and hydrologic uncertainty on future flood risk assessments. *Hydrological Processes*, *29*(12), 2823–2839. https://doi.org/10.1002/hyp.10409

Taner, M. Ü., Ray, P., & Brown, C. (2017). Robustness-based evaluation of hydropower infrastructure design under climate change. *Climate Risk Management*, *18*, 34–50. https://doi.org/10.1016/j.crm.2017.08.002

Tebaldi, C., & Friedlingstein, P. (2013). Delayed detection of climate mitigation benefits due to climate inertia and variability. *Proceedings of the National Academy of Sciences*, *110*(43), 17229–17234. https://doi.org/10.1073/pnas.1300005110

van den Hurk, B. J. J. M. (2022). Impact-Oriented Climate Information Selection. *Springer Climate*, 27–32. https://doi.org/10.1007/978-3-030-86211-4_4

van den Hurk, B. J. J. M., van Oldenborgh, G. J., Lenderink, G., Hazeleger, W., Haarsma, R., & de Vries, H. (2014). Drivers of mean climate change around the Netherlands derived from CMIP5. *Climate Dynamics*, *42*(5), 1683–1697. https://doi.org/10.1007/s00382-013-1707-y

van der Wiel, K., Beersma, J., van den Brink, H., Krikken, F., Selten, F., Severijns, C., Sterl, A., van Meijgaard, E., Reerink, T., & van Dorland, R. (2024). KNMI'23 Climate Scenarios for the Netherlands: Storyline Scenarios of Regional Climate Change. *Earth's Future*, *12*(2), e2023EF003983. https://doi.org/10.1029/2023EF003983

van Verseveld, W., Weerts, A. H., Visser, M., Buitink, J., Imhoff, R. O., Boisgontier, H., Bouaziz, L., Eilander, D., Hegnauer, M., ten Velden, C., & Russell, B. (2024). Wflow_sbm v0.7.3, a spatially distributed hydrological model: From global data to local applications. *Geoscientific Model Development*, *17*(8), 3199–3234. https://doi.org/10.5194/gmd-17-3199-2024

Virtanen, P., Gommers, R., Oliphant, T. E., Haberland, M., Reddy, T., Cournapeau, D., Burovski, E., Peterson, P., Weckesser, W., Bright, J., van der Walt, S. J., Brett, M., Wilson, J., Millman, K. J., Mayorov, N., Nelson, A. R. J., Jones, E., Kern, R., Larson, E., … van Mulbregt, P. (2020). SciPy 1.0: Fundamental algorithms for scientific computing in Python. *Nature Methods*, *17*(3), 261–272. https://doi.org/10.1038/s41592-019-0686-2

Watterson, I. G. (2005). Simulated changes due to global warming in the variability of precipitation, and their interpretation using a gamma-distributed stochastic model. *Advances in Water Resources*, *28*(12), 1368–1381. https://doi.org/10.1016/j.advwatres.2004.11.016

Watterson, I. G., & Dix, M. R. (2003). Simulated changes due to global warming in daily precipitation means and extremes and their interpretation using the gamma distribution. *Journal of Geophysical Research: Atmospheres*, *108*(D13). https://doi.org/10.1029/2002JD002928

Wilby, R. L., & Wigley, T. M. L. (2002). Future changes in the distribution of daily precipitation totals across North America. *Geophysical Research Letters*, *29*(7), 39-1-39–4. https://doi.org/10.1029/2001GL013048

Zappa, G., & Shepherd, T. G. (2017). Storylines of Atmospheric Circulation Change for European Regional Climate Impact Assessment. *Journal of Climate*, *30*(16), 6561–6577. https://doi.org/10.1175/JCLI-D-16-0807.1

Appendix A: Hydrological Validation
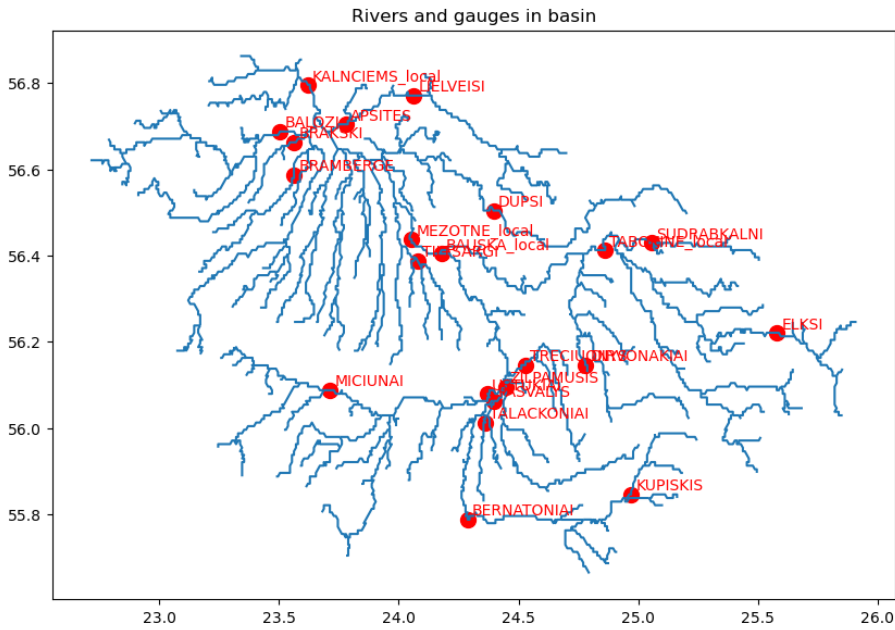
Figure A.1: A map of the Lielupe basin rivers (in blue) with Initial stations in the basin that are used to validate the hydrological model indicated by red dots annotated with their name.
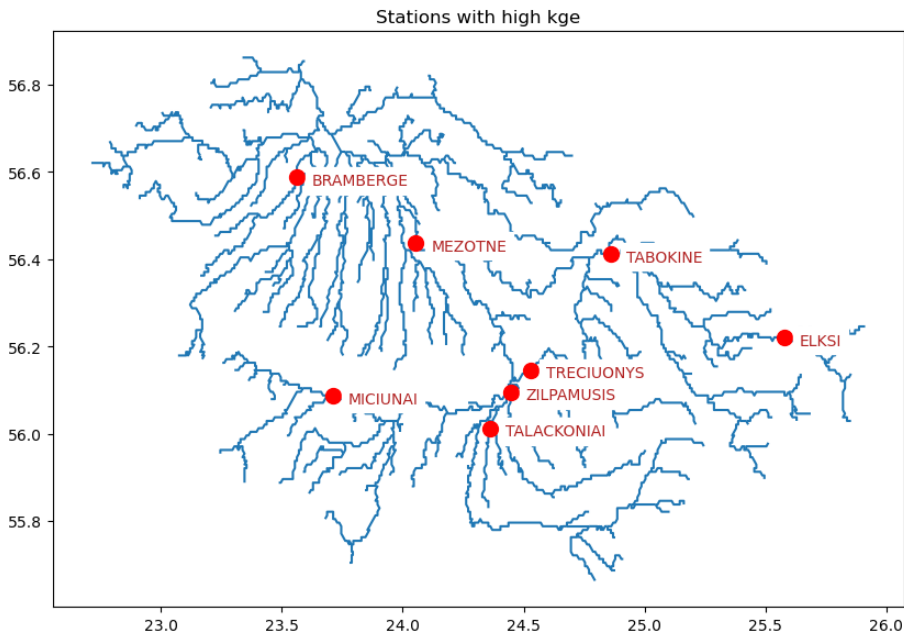

Figure A.2: A map of the Lielupe basin rivers (in blue) with stations in red with high enough Kling-Gupta Efficiency (>= 0.5) to consider. The names of the stations are annotated in red.
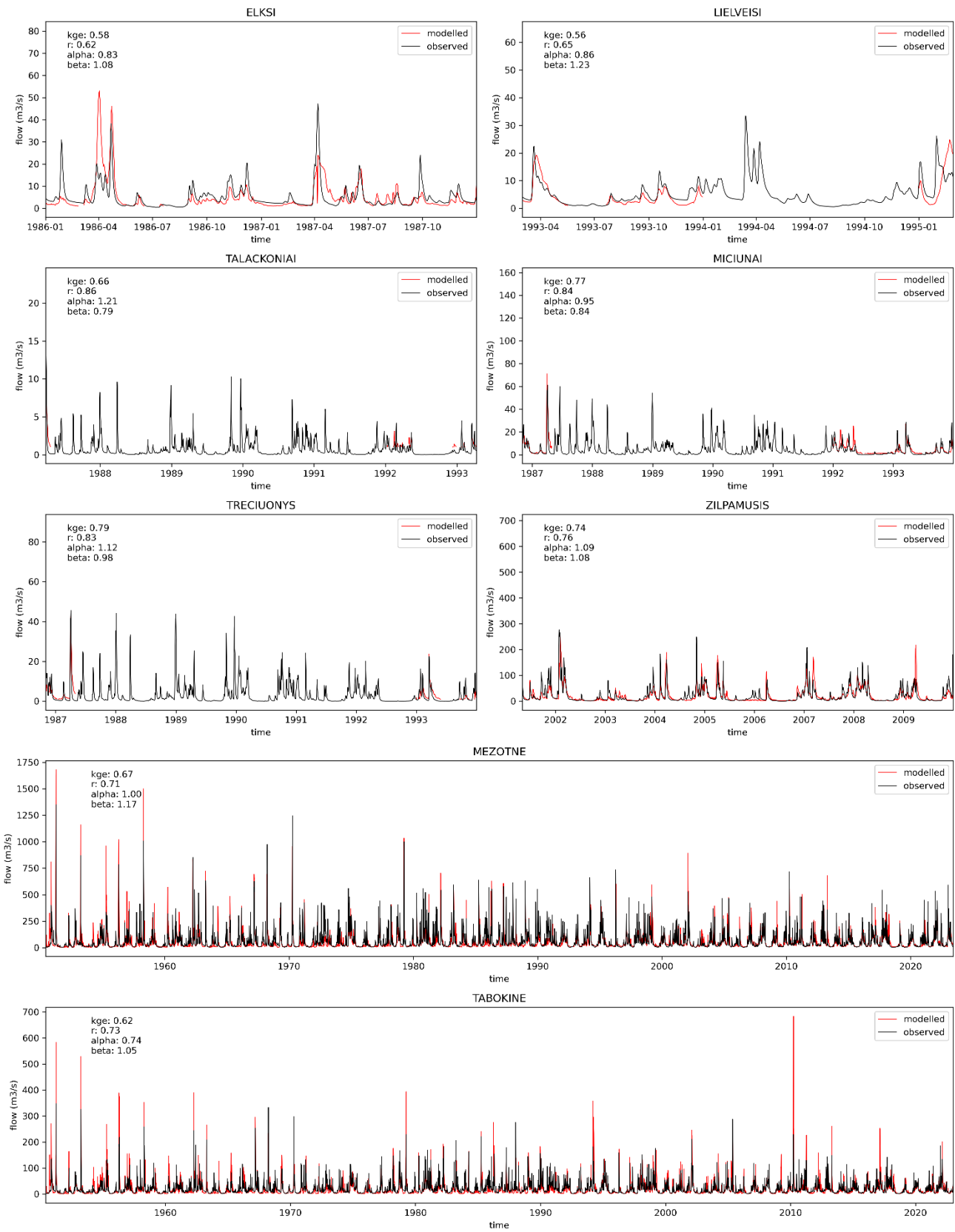
Figure A.3: Available time period of historical flows versus modelled flow. Simulated flows from June 1950 to June 2023

Appendix B: Weather generator

In this appendix, we highlight the use of the weather generator by Steinschneider & Brown (2013). This weather generator is a key component of the study as it allows us to create a high-resolution time series with a consistent sequence of events across different climate futures. These requirements are unfilled in gridded GCM time series. High resolution is vital for meaningful hydrological modelling in the region. A consistent sequence of events is essential to analyse and compare the effect of changes in Climate Impact Drivers (CIDs) signalled by GCM projections.

First, we show the weather generator's applicability to the Latvian case by exploring its ability to replicate historical climate statistics in the 100-year synthetic baseline time series used. Secondly, we describe the retrieval of climate projections for the various CIDs used in this study and show how these changes influence the synthetic baseline time series. Lastly, we dive into the hydrological response of discharge extremes due to these applied changes to the synthetic baseline time series.

Replication of historical climate statistics

The following figures highlight the weather generator's applicability to the Lielupe case study. We determine the weather generator's applicability by analysing its ability to replicate the region's historical climate statistics in the 100-year-long synthetics baseline time series. Here, the historical climate statistics are retrieved from the observed ERA5 dataset between 1940 and 2014. We look at monthly temperature and precipitation mean, standard deviation and skew (Figures B.1 and B.2), number of dry and wet days (Figure B.3), and dry and wet spell length (Figure B.4). We also compare observed and synthetic time series correlations across grid cells (Figure B.5). Finally, we observe and compare daily grid cell means and standard deviation per month for temperature and precipitation (Figure B.6 and B.7).

We find good replication of the monthly statistics provided in Figures B1. and B.2. This means that the season is well replicated, and we can start to adjust the seasonal average temperature and precipitation and coefficient of variation statistics in a meaningful way. Also, the dry and wet spell days and duration are replicated well across the region and seasons (Figures B.3 and B.4). In Figure B.4, we find a slight underestimation of the baseline wet spell length compared to observations; these underestimations are under one day. We conclude that the synthetic baseline time series replicates the historic wet and dry spell conditions well. Figure B.5 highlights that the cross-basin correlation of temperature and rainfall in the synthetic baseline also matches the observed correlations. In Figure B.6 we note that the grid cell means also match historical observation. In Figure B.7, the standard deviation for precipitation is well captured. However, we note a slight underestimation (<0.5 °C) of temperature variability in situations of high monthly standard deviations (>5 °C). Figure B.1, however, shows that overall, the overall monthly temperature variability in the basin is well captured and explored. Since basin-wide temperatures on large-scale snow accumulation and melt are dominant for large-scale flood patterns in the region, we believe this slight underestimation on a few grid cells does not undermine the analysis.

Overall, we conclude that the weather generator can replicate historical patterns well. This allows us to apply it to our case study and subject a synthetic baseline time series to a set of climate changes for temperature and precipitation.
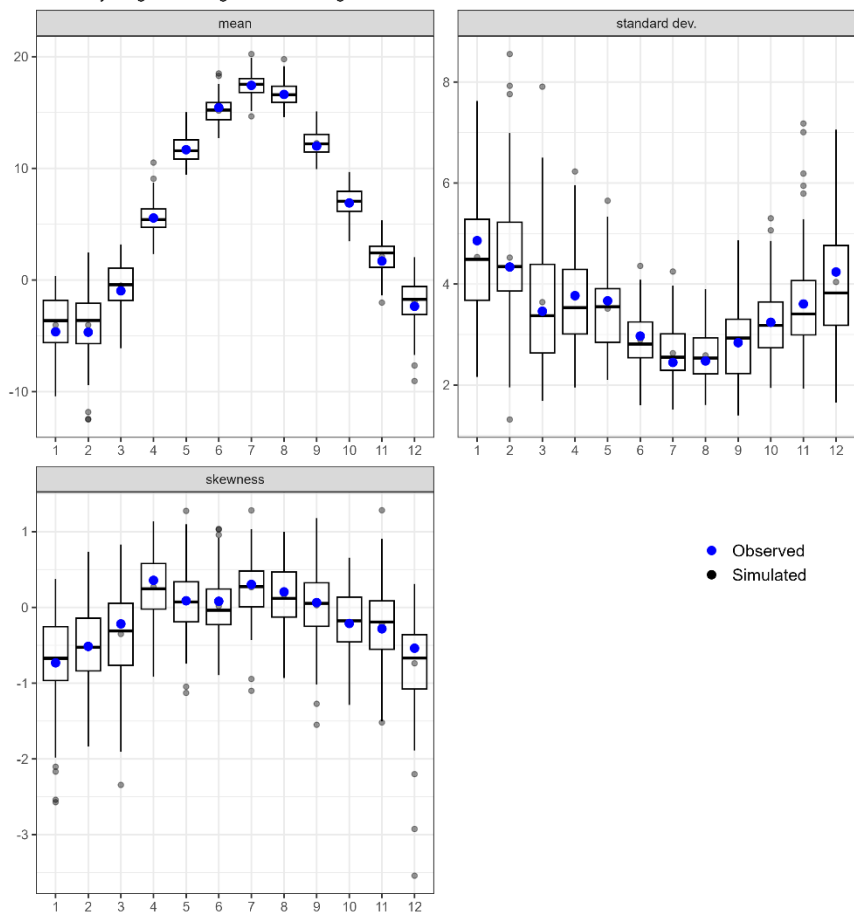
Figure B.1: Monthly variability of temperature. This figure compares the monthly variability of temperature simulated by the stochastic weather generator (black points) to observed data (blue points) across all grid cells. The mean (top left) shows monthly averages, with box plots indicating the range in the synthetic baseline simulation, while the dots represent observed and simulated values. The standard deviation (top right) reflects monthly temperature variability, and the skewness (bottom) demonstrates the distribution's asymmetry, showing how symmetric or skewed the temperature values are.

Monthly variability of precip
Monthly means from all stochastic simulations compared to the observed values.
Variability range is averaged accross all grid cells.
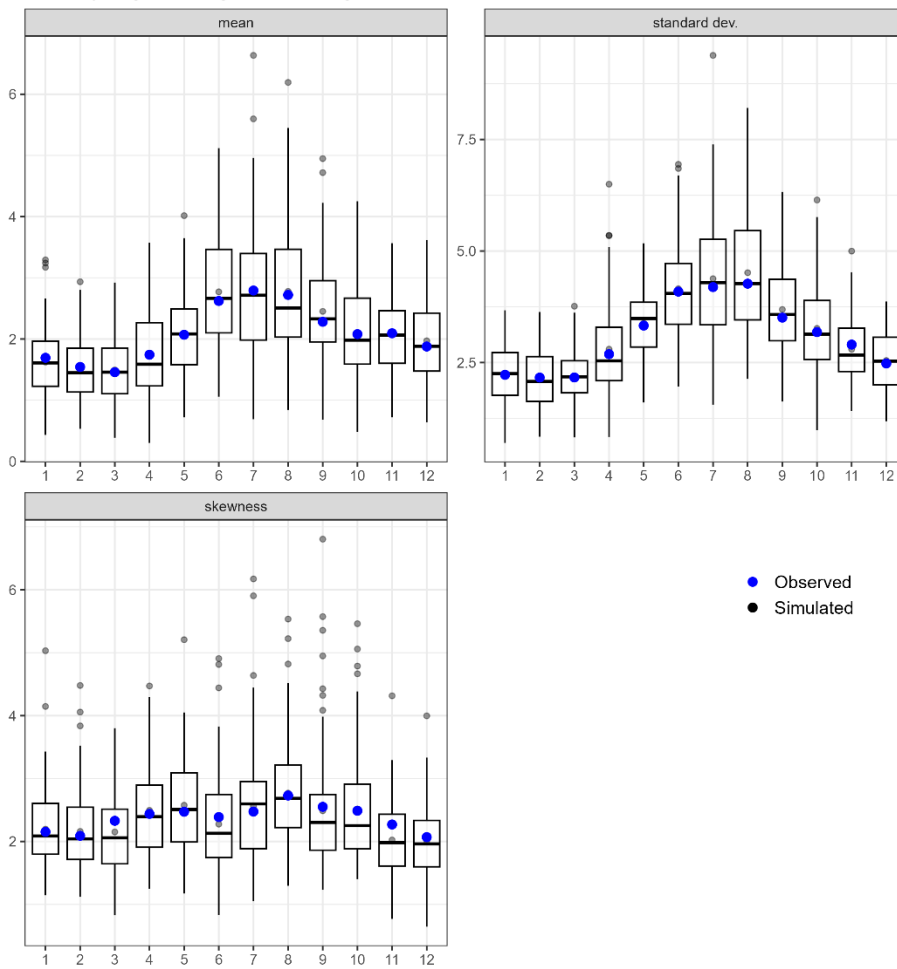
Figure B.2: Monthly variability of precipitation. This figure depicts the monthly variability of precipitation, comparing the weather generator's simulations (black points) to observations (blue points). The mean (top left) represents monthly precipitation averages, while box plots show the spread of values in the synthetic baseline. The standard deviation (top right) highlights monthly variability, and the skewness (bottom) captures the asymmetry of the precipitation distribution across months.

Average number of dry and wet days per month across all grid cells
Stochastic simulation range is shown against the observed values
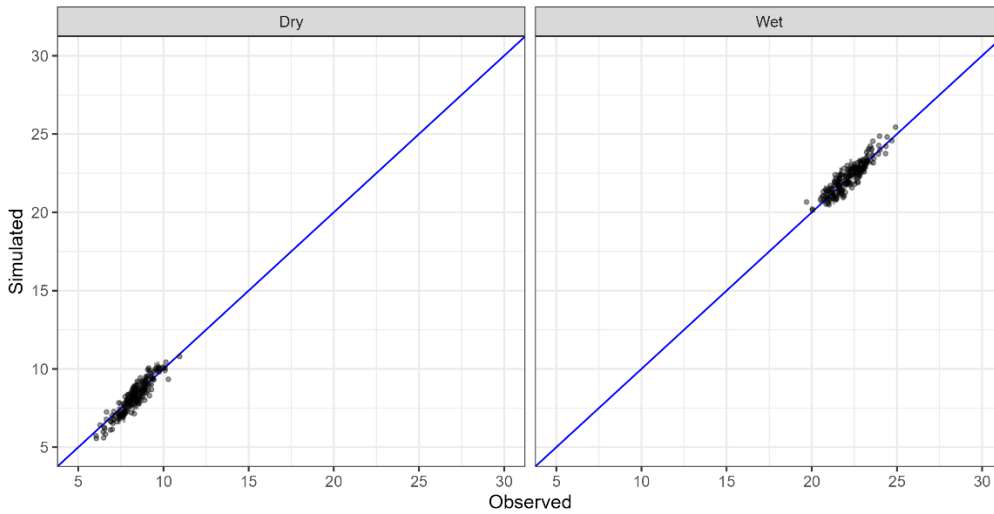
Figure B.3: Average number of dry and wet days per month across all grid cells. This figure compares the simulated versus observed average number of dry (left) and wet (right) days per month across multiple grid cells. The blue 1:1 line represents perfect agreement between the simulated and observed values. The clustering of points around the line indicates a strong match between simulated and observed dry and wet day frequencies, with some minor deviations.

Average length of dry and wet spells per month and grid cell (days)
Range and median of all stochastic simulations are shown against the observed values
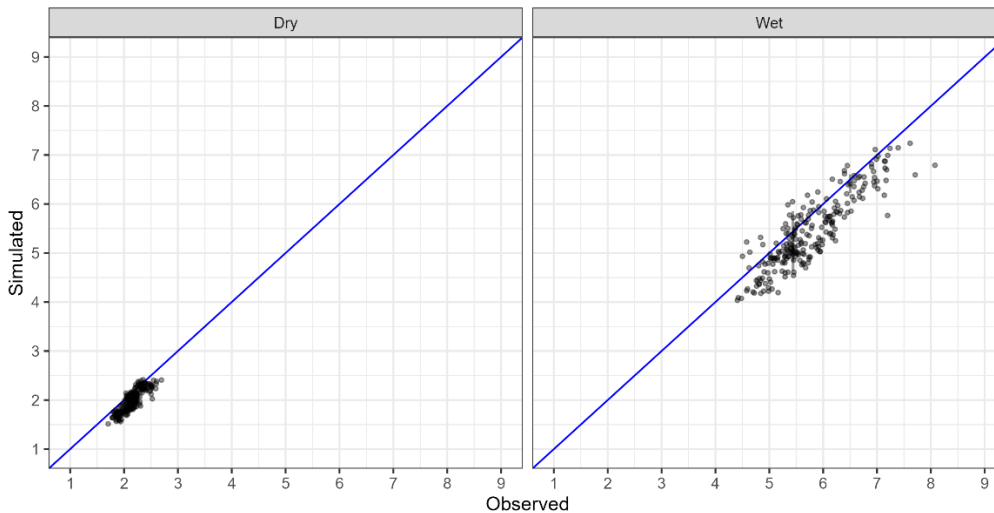
Figure B.4: Average length of dry and wet spells per month and grid cell (days). This figure shows the comparison between simulated and observed average lengths of dry (left) and wet (right) spells per month across grid cells. The blue 1:1 line indicates perfect agreement between the simulated and observed spell durations. The points clustering around the line suggest good correspondence between simulations and observations, particularly for wet spells, with slightly more variability for dry spell lengths.

Intersite correlations for all variables

Stochastic simulation range is shown against the observed values for each grid cell.
Correlations are calculated over the entire period.
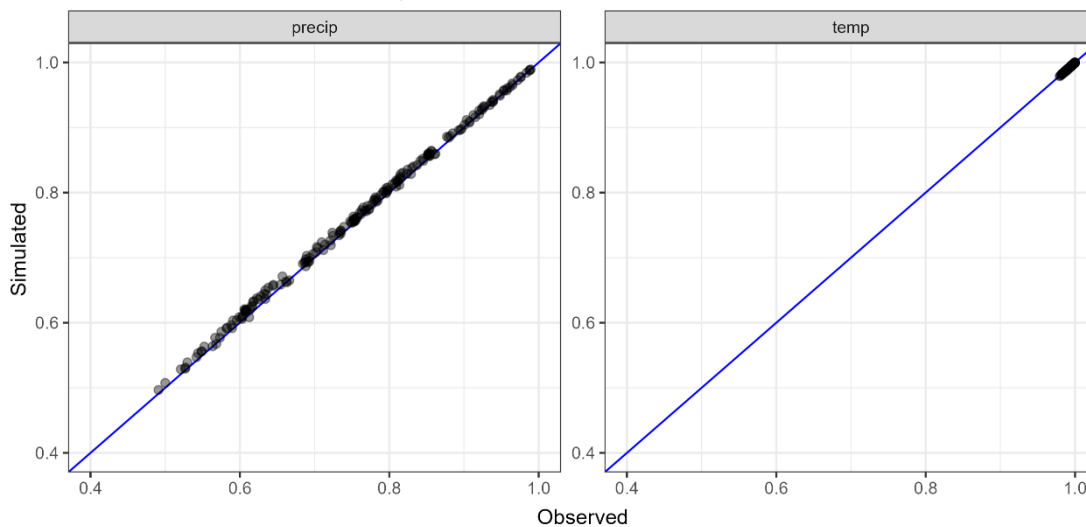
Figure B.5: Intersite correlation for daily variables across grid cell.: This figure compares intersite correlations of precipitation (left) and temperature (right) from the simulated stochastic weather generator (y-axis) with observed values (x-axis) across all grid cells. The blue 1:1 line represents perfect agreement. The closeness of the points to the line indicates how well the simulation preserves spatial correlation patterns of the observed data across grid cells

Mean of daily variables calculated across each month and grid cell

Range from all stochastic simulations are shown against the observed values
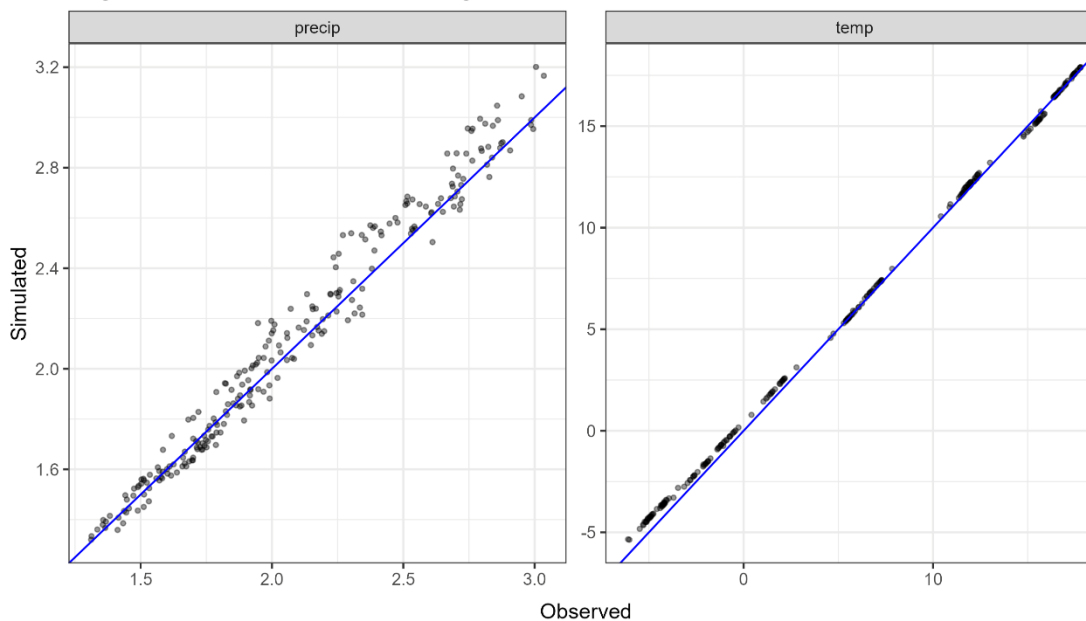
Figure B.6: Mean of daily variables across all grid cells and months. The figure compares the mean values of daily precipitation (left) and temperature (right) simulated by the stochastic weather generator (y-axis) against the observed data (x-axis) across multiple grid cells and months. The blue 1:1 line indicates a perfect match between simulated and observed values. The scatter of the points represents variability in simulations relative to observations.

Standard deviation of daily variables calculated across each month and grid cell
Range from all stochastic simulations are shown against the observed values
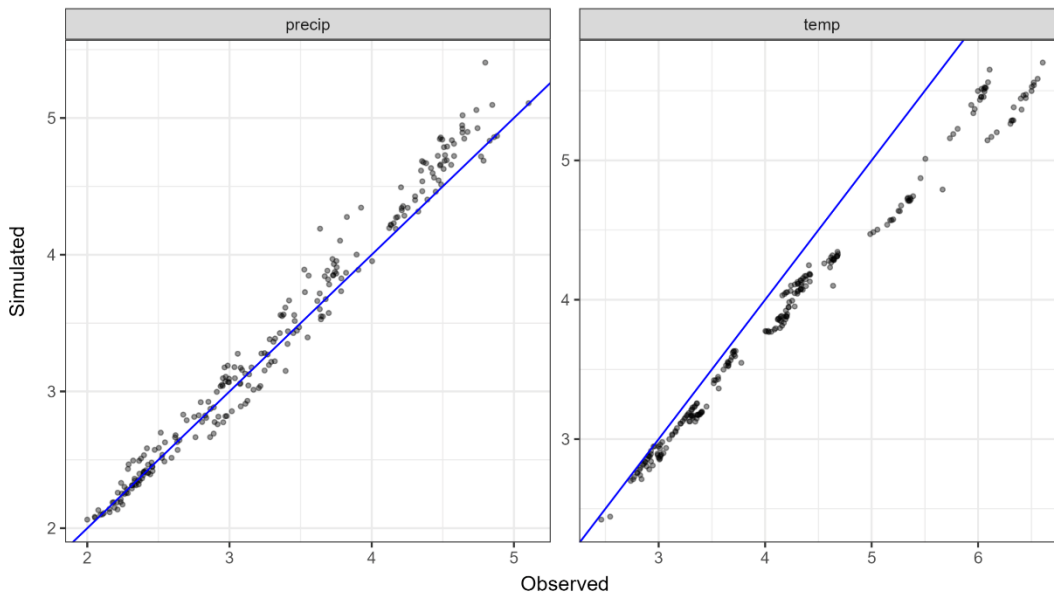
Figure B.7: Standard deviation of daily variables across all grid cells and months. This figure shows the comparison of the standard deviation of daily precipitation (left) and temperature (right) simulated by the weather generator (y-axis) against the observed standard deviations (x-axis) for multiple grid cells and months. Points close to the blue 1:1 line indicate a good match between simulated and observed variability, while deviations suggest areas where the model underestimates or overestimates variability.

Retrieving and applying climate signals

In this section, we dive into how climate signals are retrieved and how we apply them to the synthetic baseline time series. We start by defining the region where we want to retrieve GCM projection data from the Copernicus Climate Data Store. As the river basin we are investigating is relatively small, we wanted to extract GCM climate data for a larger region to gain a more robust climate signal. Therefore, we create a correlation mask to extract a climate signal only where ERA5 grid cell time series have a correlation of 0.6 or higher when compared to the grid cell at the basin's centre. In Figures B.8 and B.9, correlation regions are shown for precipitation and temperature at various correlation thresholds. We see that temperature across Europe is highly correlated while precipitation has a faster area size dropoff when correlation increases thresholds. The GCM area mask to extract climate data is determined by precipitation patterns.

After extracting the climate signals using the method described in the main text Section 2.3.1, we end up with a collection of seasonal signals provided in Figure B.10. Here, we show a scatter plot of individual GCM projections for seasonal changes in each CID. We find a large range of potential future outcomes in the region. Not only is there uncertainty in the magnitude of change, but there are also contradictions in the sign of change. For the CV value, each of the seasons has contradictory signals, and for precipitation, there is signal uncertainty in the summer (JJA) and autumn (SON) months. Table B.1 highlights the ranges between minimum and maximum projected changes for each of the seasonal CIDs. As described in the main text Section 2.3.1, these changes are sampled and applied to the synthetic weather time series.

The baseline synthetic weather time series from previous section are adjusted using the approach described in Steinschneider & Brown (2013). Temperature changes are applied by adding a delta factor for the specific seasons we are considering in the climate stress test. For example, in Figure B.11 we consider a 7.1 °C increase in temperature in spring. Each temperature value in the time series is increased by 7.1 °C. For precipitation changes, we apply a quantile mapping procedure as illustrated in Figure B.12. This procedure allows us to remap precipitation values of the synthetic baseline (corresponding to historical conditions), to a climate scenario. We use the known cumulative distribution function (CDF) of the baseline gamma distribution that describes rainfall and adjust the CV and mean of the CDF to align with the climate future of interest. With both these distributions known, baseline rainfall values are remapped by finding new rainfall values in the new climate scenario CDF that correspond to the same probability value. Using this approach, we can account for changes in future precipitation patterns. In Figure B.11 we can see the influence of such quantile mapping on spring precipitation. For an interactive experience of time series adjustments go to the online Github page: https://github.com/TBuskop/Enhancing-impact-exploration/blob/main/Applying%20climate%20changes%20to%20time%20series.ipynb
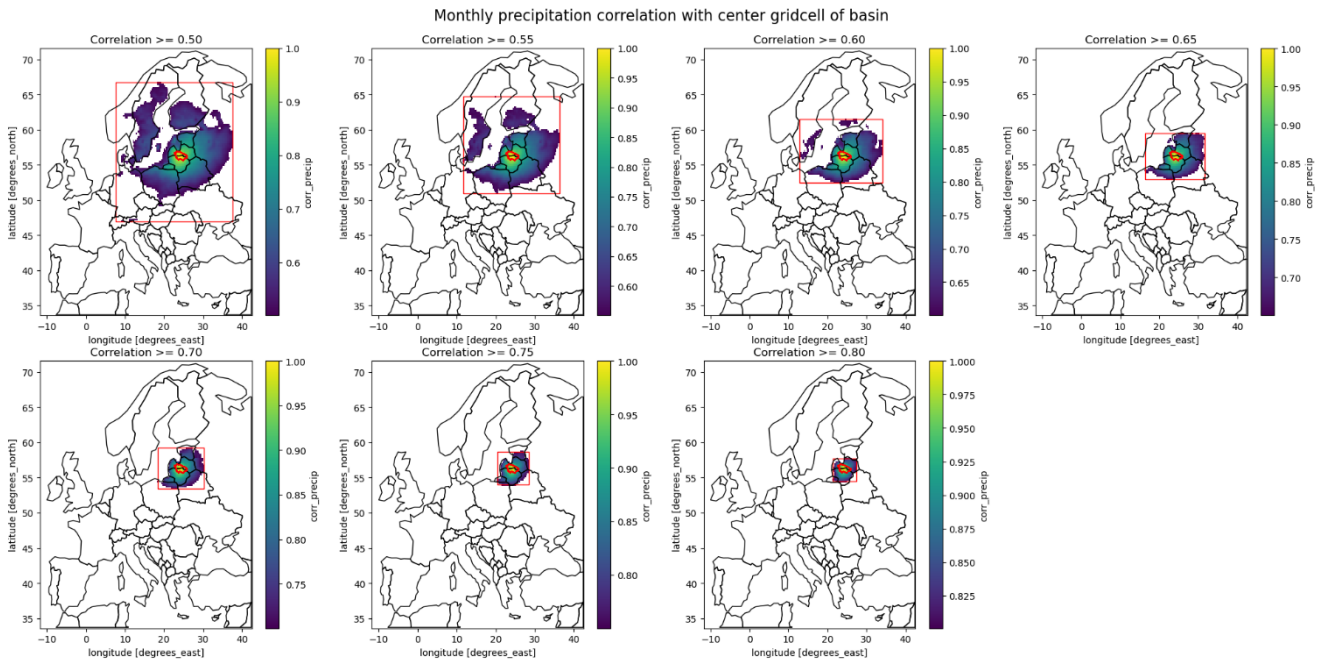
Figure B.8: Correlation of monthly averaged precipitation time series of each grid cell when compared to the time series of the grid cell at the centre of the Lielupe basin. The heatmap shows the correlation value. The red square indicates the boundary of the region where the correlation condition is met, and the red shape indicates the boundary of the Lielupe basin. Country borders are shown in black.
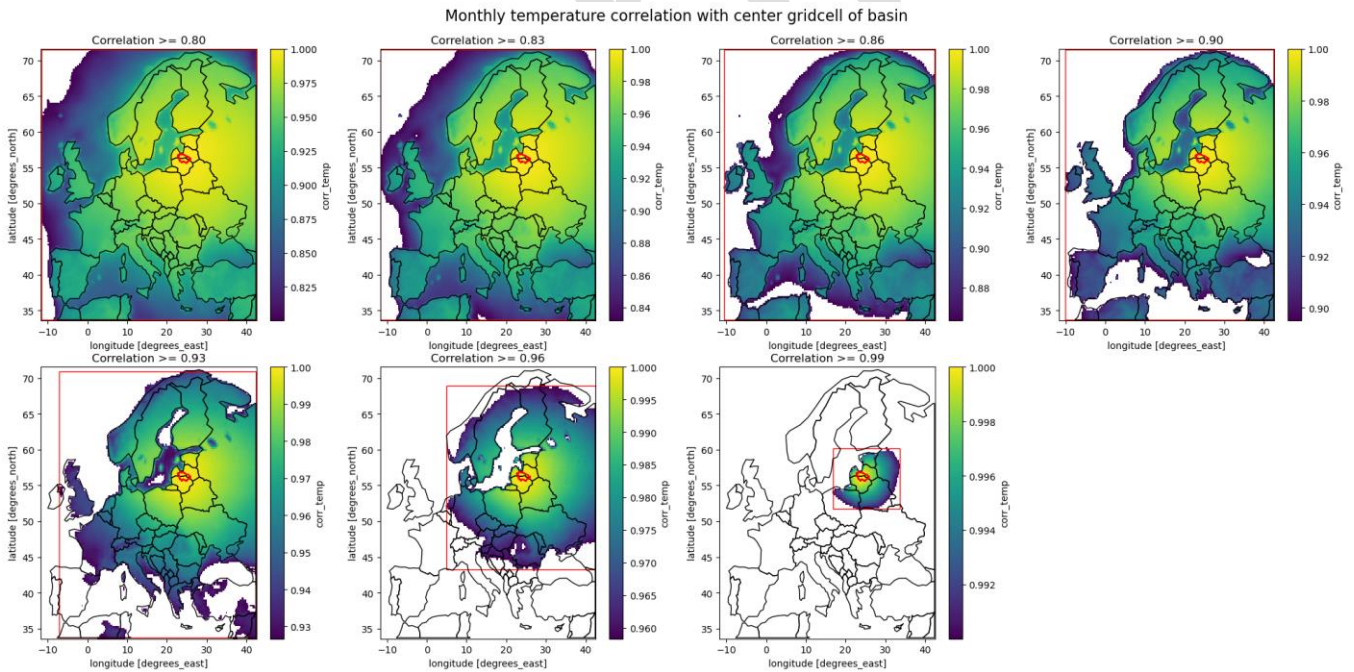

Figure B.9 Correlation of monthly averaged temperature time series of each grid cell when compared to the temperature time series of the grid cell at the centre of the Lielupe basin. The heatmap shows the value of correlation value. The red square indicates the boundary of the region where the correlation condition is met, and the red shape indicates the boundary of the Lielupe basin. Country borders are shown in black.
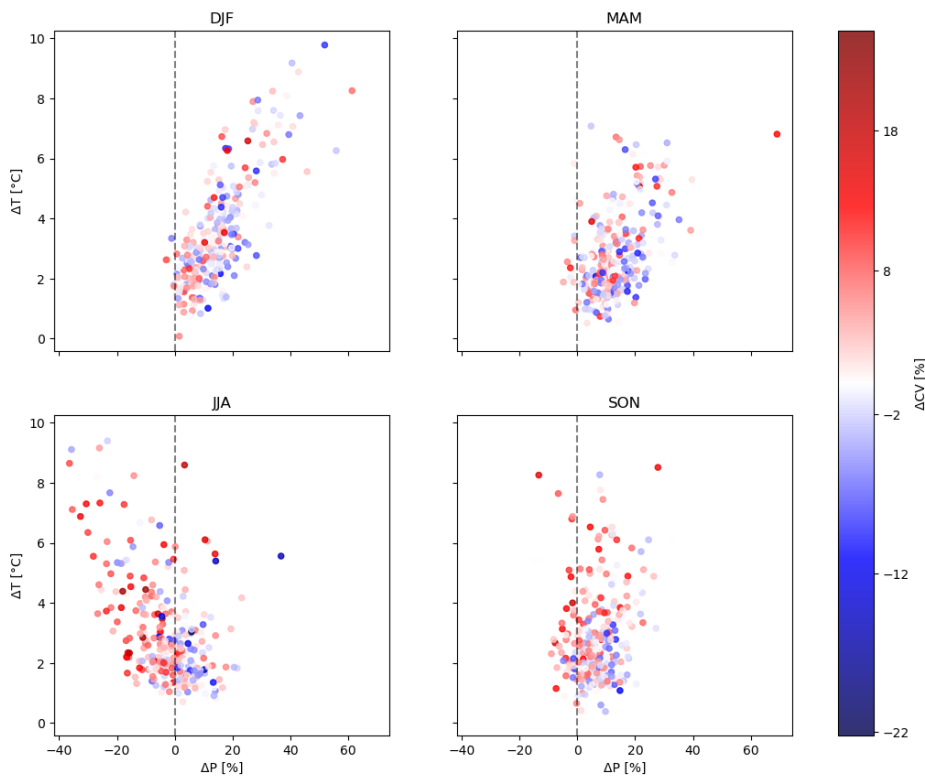
Figure B.10: Extracted climate information in the specified region. Changes for average **temperature (ΔT)**, average **precipitation (ΔP)** and precipitation variability (ΔCV) are provided **across four seasons: DJF (winter), MAM (spring), JJA (summer), and SON (autumn).** Each dot represents an SSP, timeframe, model, and ensemble combination.**Table B.1:** Seasonal ranges for selected climate features given in percentages fo changes in average. precipitation (ΔP) and precipitation variability (ΔCV) and absolute degree Celsius changes in average temperature (ΔT).

season	ΔT		ΔP		ΔCV	
	min	max	min	max	min	max
DJF	0.1	9.8	-3.0	61.3	-11.2	16.8
MAM	0.5	7.1	-4.8	69.1	-12.7	16.6
JJA	0.7	9.4	-36.4	36.7	-22.2	22.2
SON	0.4	8.5	-13.8	32.6	-11.5	25.2
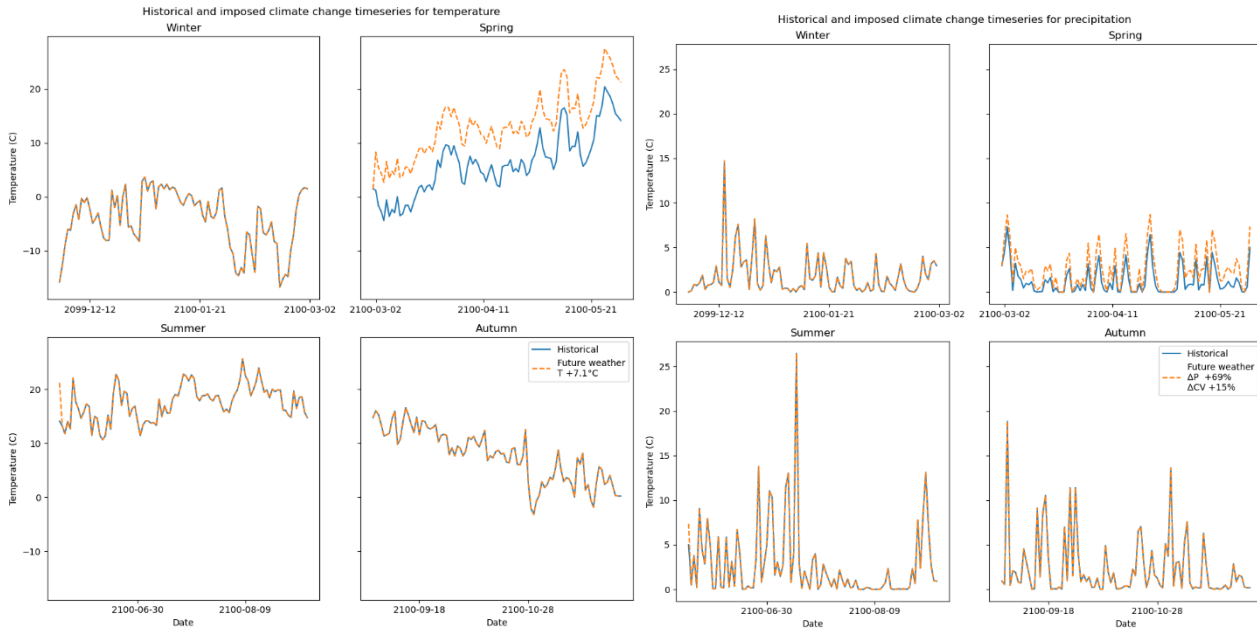
Figure B.11: Adjusted weather time series for a single scenario where spring temperature, precipitation mean and coefficient of variation (CV) are adjusted.
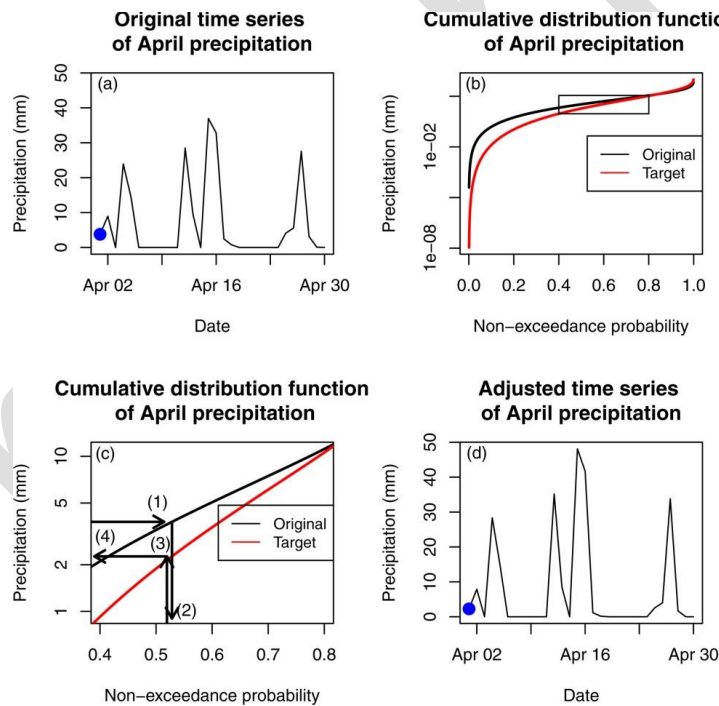

Figure B.12: Figure and caption taken as is from Steinschneider & Brown (2013) to illustrate the quantile mapping procedure. The quantile mapping procedure to adjust daily, nonzero precipitation values. (a) A sample of an original time series of April precipitation simulated by the weather generator. The blue point represents a sample precipitation value to be adjusted. (b) The cdf for the fitted gamma distribution to the original simulation of April precipitation (black), as well as the target cdf used to make the adjustments (red). (c) The rectangle delimits an inset, shown in detail. Here, the precipitation value represented by the blue point in Figure 2a is mapped to a new precipitation value via four steps. (d) The new, adjusted precipitation time series, including the adjusted point (blue), is shown.

Hydrological response under new climate conditions

Using the newly created weather timeseries we can stress test the system for combination of climate change signals and extract discharge extremes for various return periods as described in Section 2.3.3. In Figure B.12 we can analyse the flow return period curve for every climate stress test and compare it to the synthetic historical baseline. We can notice a general upward

shift in flows for return periods across stress tests. In Figure B.14 we can see the effect of stress test on each historical individual yearly maxima. In Figure B.15 we analyse the shifts in return period discharge changes across stress tests and see that the median of stress test do not create a large difference, however, there are some that do create large differences. This enforces the superstition that not all stress tested climate variables matter in changing the discharge.
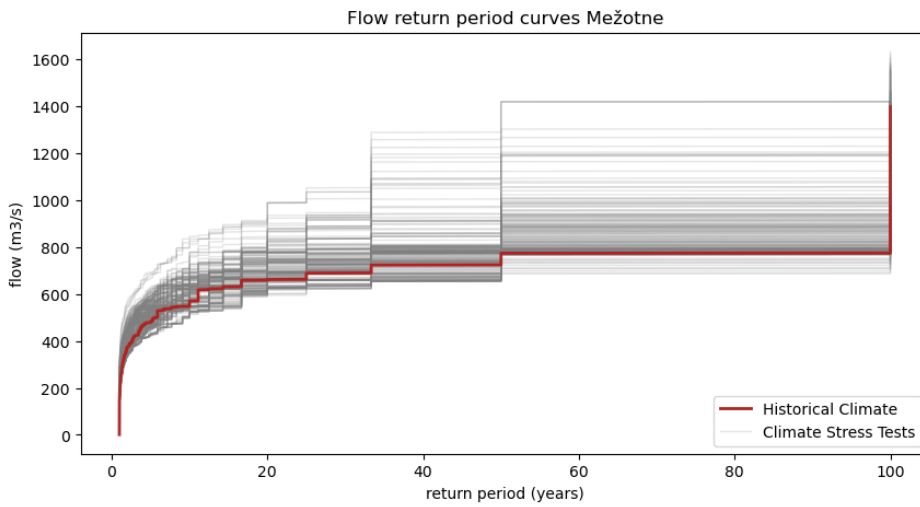

Figure B.13: Flow return periods for the historical climate realisation and 256 climate scenarios.
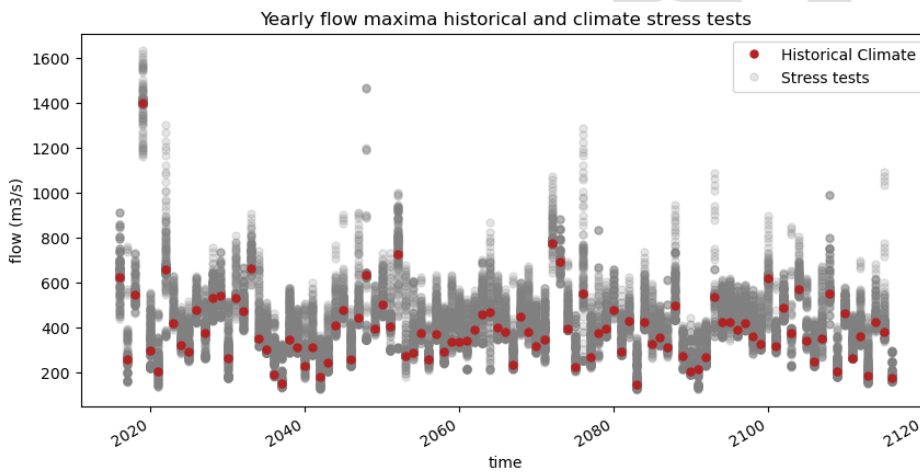
Figure B.14: The yearly flow maxima of seasonal stress tests show the historical climate. The yearly maxima is in red, and the range of stress test maxima is in grey.
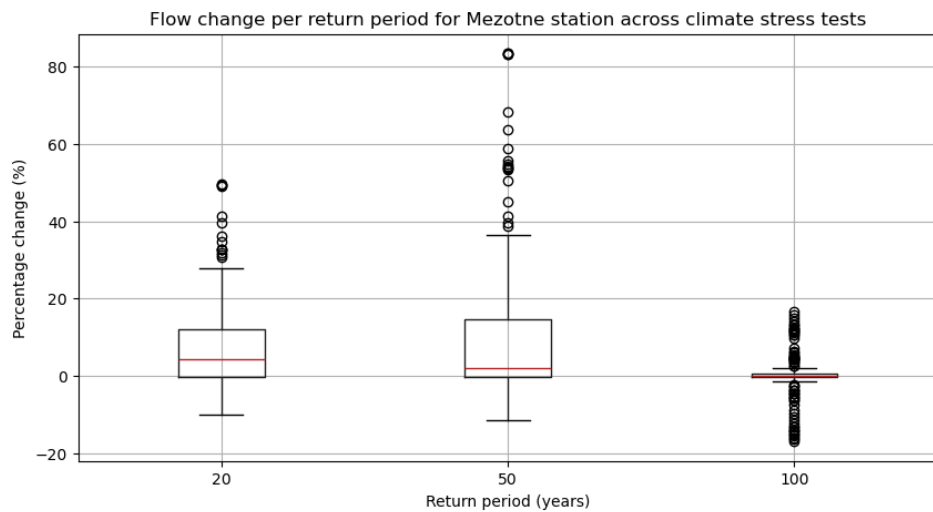
Figure B.15: Boxplot of stress test outcomes for the return periods of interest.

Appendix C: Explaining hydrological response to changing climate variables
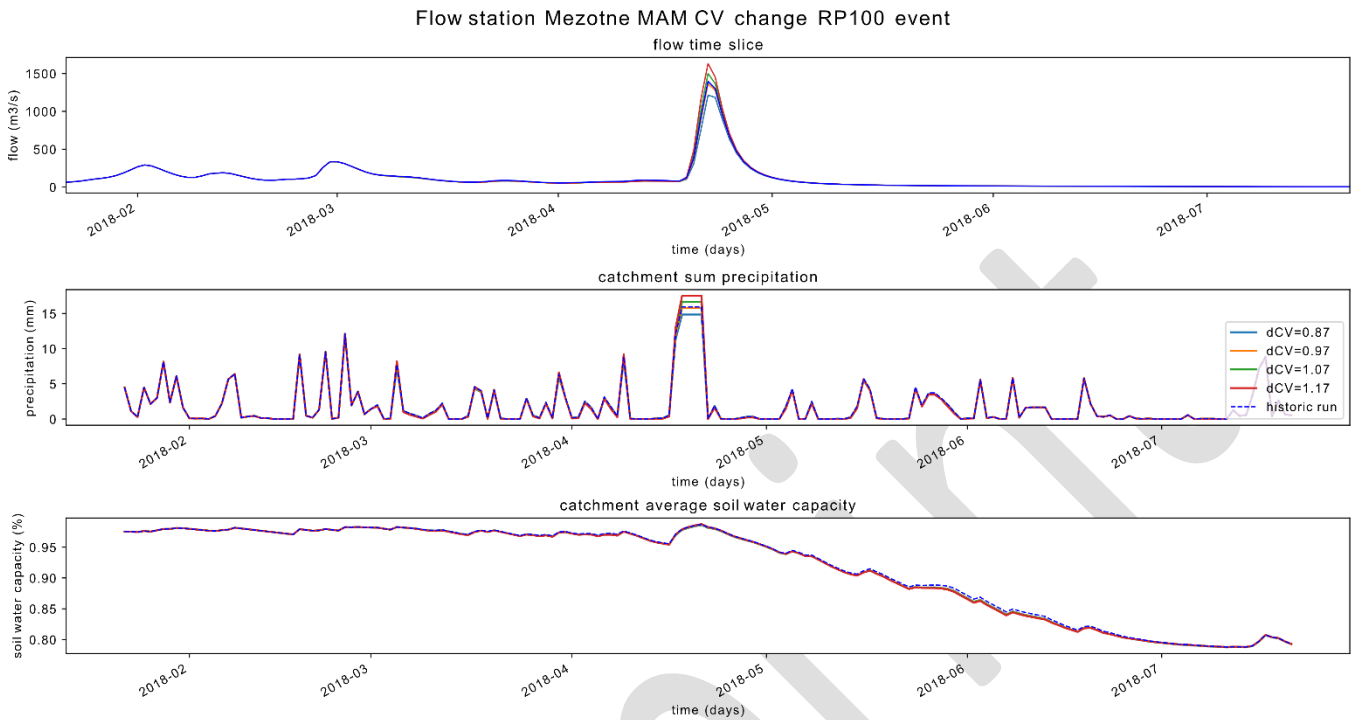
Flow station Mezotne MAM CV change RP100 event

Figure C.1 100-year return period flow event under changing rainfall variability in the spring season.

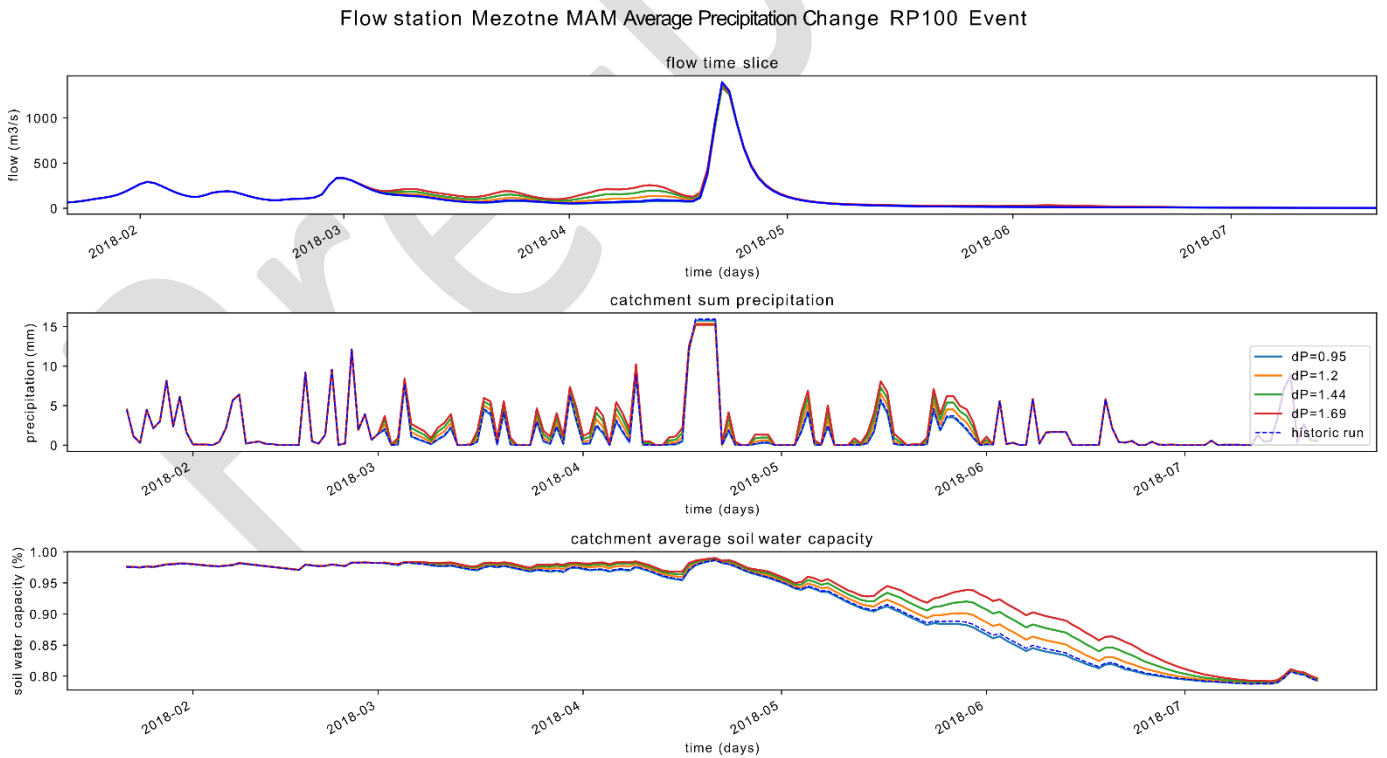## Flow station Mezotne MAM Average Precipitation Change RP100 Event

Figure C.2 100-year return period flow event under changing average rainfall in the spring season.

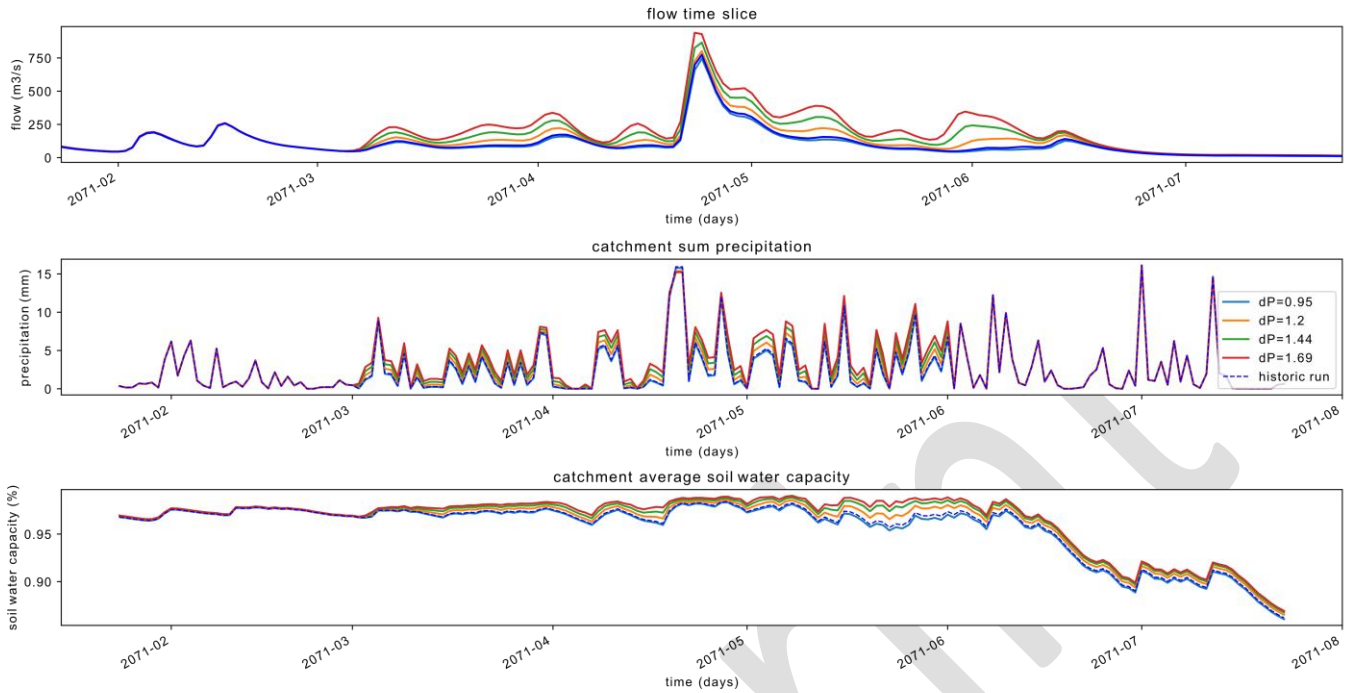## Flow station Mezotne MAM change average precipitation for RP50 event

Figure C.3 50-year return period flow event under changing average rainfall in the spring season.

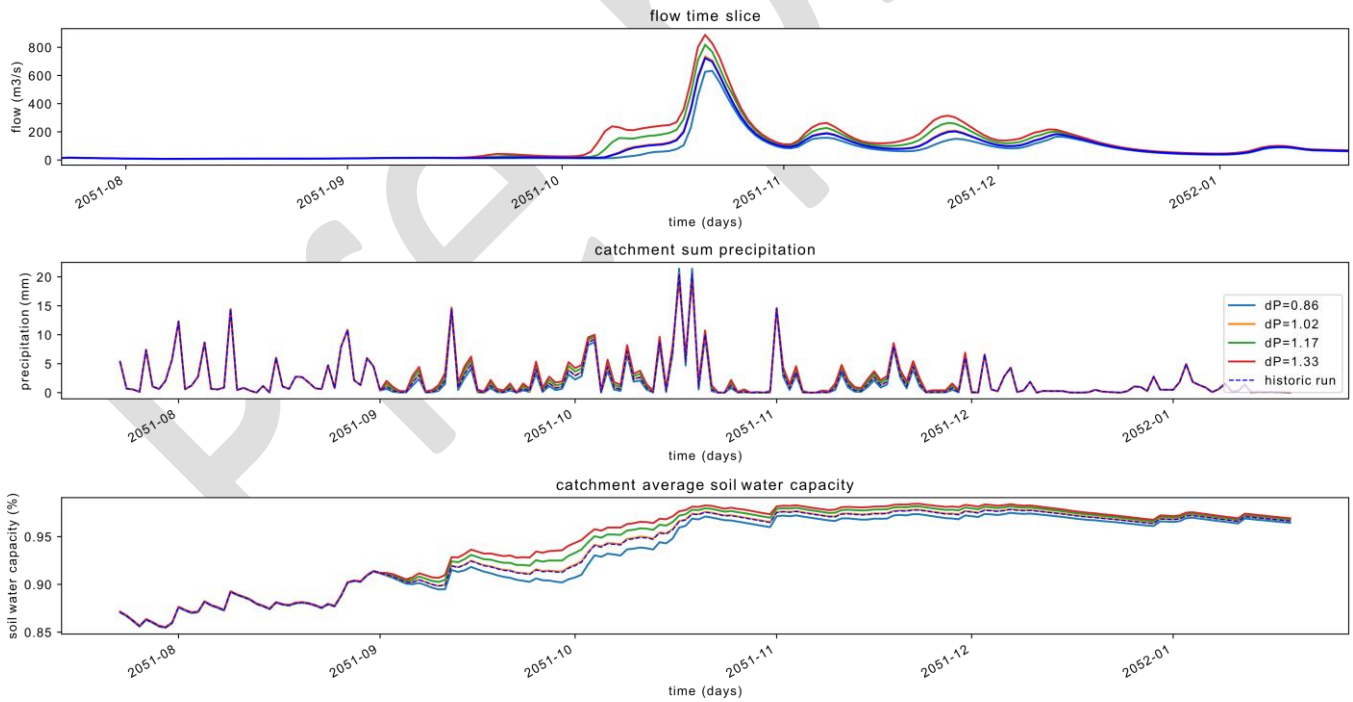## Flow station Mezotne SON change in average precipitation on RP20 flow

Figure C.4 20-year return period flow event under changing average rainfall in the autumn season.
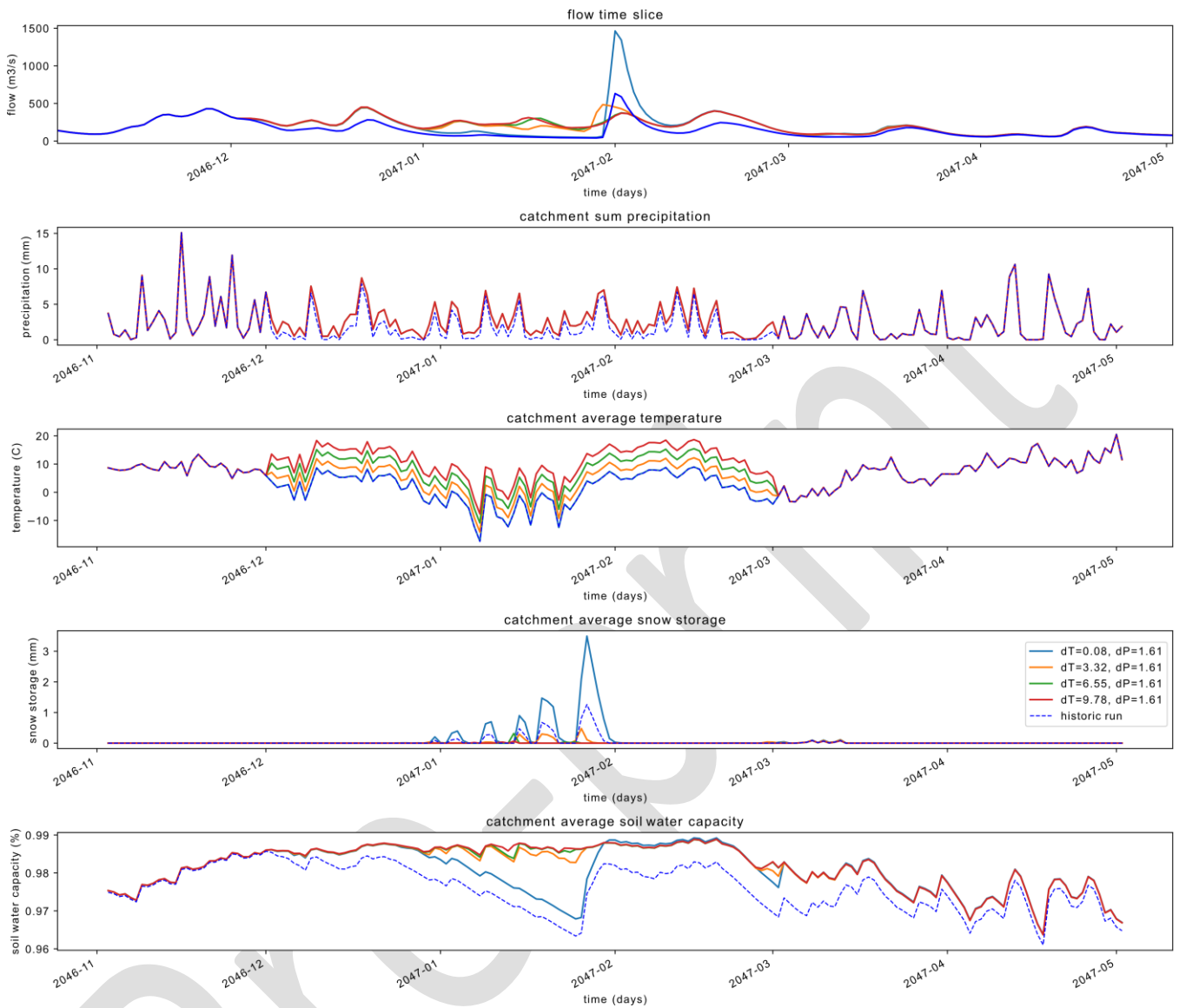
Figure C.5 Discharge change due to snowmelt under changing winter conditions.

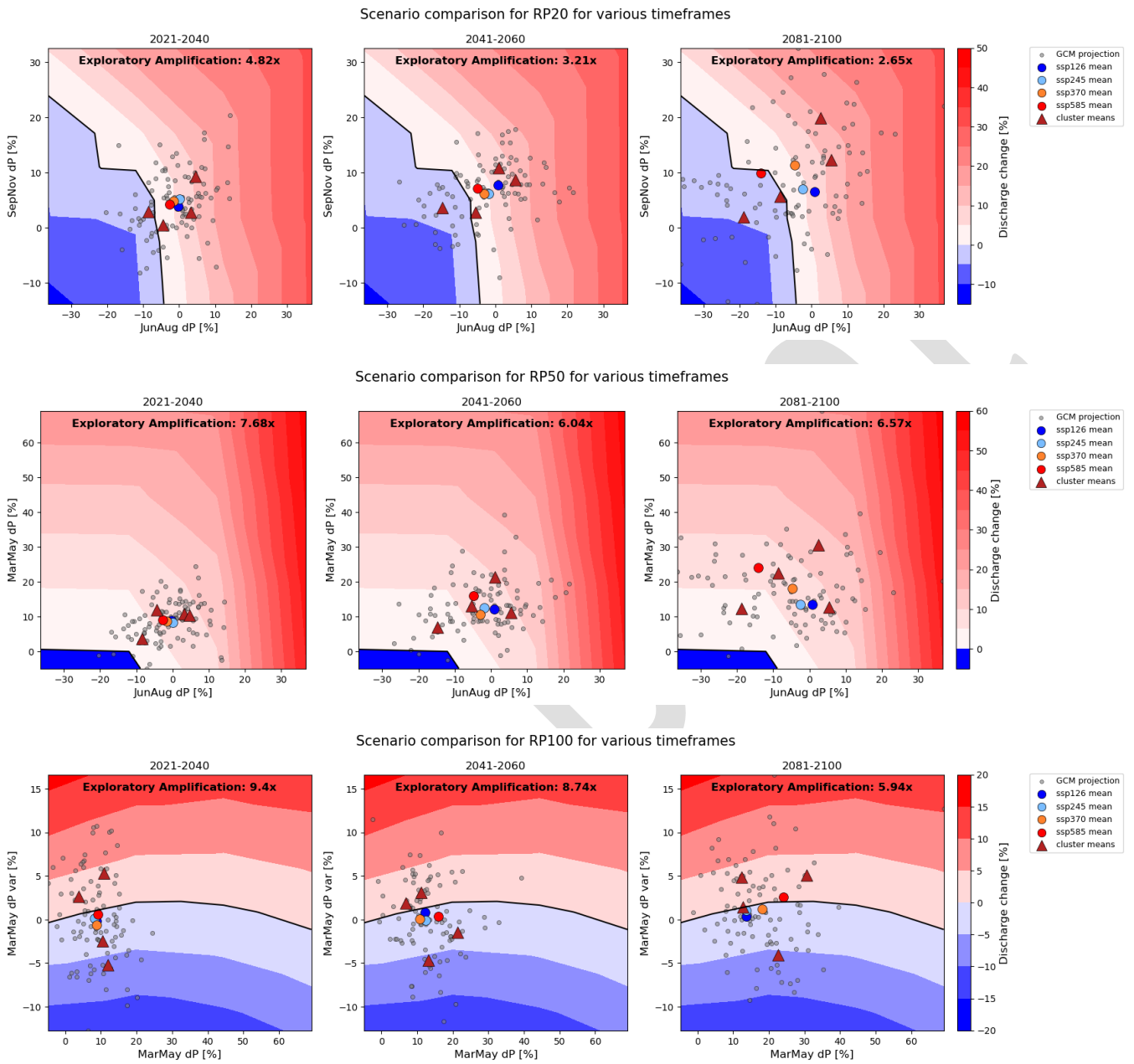# Appendix D: Exploratory power for each RP and timeframe

Figure D.1: Response surface plots relating the impact relevant climate features to the three impact metrics (flow change for 100, 50, 20-year return period discharge) in different timeframes.

Table D.1: Table of used models and SSPs in the 2021-2040, 2041-2060, and 2081-2100 timeframes

Model Name	SSP1-2.6	SSP2-4.5	SSP3-7.0	SSP5-8.5
ACCESS-CM2	✓	✓	✓	✓
BCC-CSM2-MR	✓	✓	✓	✓
CanESM5	✓			✓
CESM2	✓	✓	✓	✓
CESM2-WACCM			✓	✓
CMCC-CM2-SR5		✓	✓	✓
CMCC-ESM2	✓	✓		✓
CNRM-CM6-1	✓	✓	✓	✓
CNRM-CM6-1-HR	✓			✓
CNRM-ESM2-1	✓	✓	✓	✓
EC-Earth3-AerChem			✓	
EC-Earth3-CC		✓		✓
FGOALS-g3	✓	✓	✓	✓
GFDL-ESM4	✓	✓	✓	✓
HadGEM3-GC31-LL	✓	✓		✓
HadGEM3-GC31-MM	✓			✓
IITM-ESM	✓	✓	✓	✓
INM-CM4-8	✓	✓	✓	✓
INM-CM5-0	✓	✓	✓	✓
IPSL-CM5A2-INCA	✓		✓	
IPSL-CM6A-LR	✓	✓	✓	✓
KACE-1.0-G	✓	✓	✓	✓
KIOST-ESM	✓	✓		
MIROC-ES2L	✓	✓	✓	✓
MIROC6	✓	✓	✓	✓
MPI-ESM1-2-LR	✓	✓	✓	✓
MRI-ESM2-0	✓	✓	✓	✓
NESM3		✓		✓
NorESM2-MM	✓	✓	✓	✓
TAI-ESM1				✓
Count	24	23	21	27